To Environ. Sci. & Technol.

Photocontrol of Goethite Crystal Facet Exposure: Implications for Phosphate Binding in Water and Sediment Systems

Bobo Xing [1], Qingqing Xue [1], Xian Li [1, 5], Nigel J. D. Graham [2], Hengzhong Zhang [3], Mark R. Wiesner [4], Wenzheng Yu [1, *]

[1] Research Center for Eco-Environmental Sciences, Chinese Academy of Sciences, Beijing 100085, China (wzyu@rcees.ac.cn)

[2] Department of Civil and Environmental Engineering, Imperial College London, South Kensington Campus, London SW7 2AZ, United Kingdom (n.graham@imperial.ac.uk)

[3] Center for High Pressure Science & Technology Advanced Research, Shanghai 201203, China (hengzhong.zhang@hpstar.ac.cn)

[4] Center for the Environmental Implications of Nanotechnology (CEINT), Duke University, Durham, North Carolina 27708, USA (wiesner@duke.edu)

[5] College of Urban and Environmental Sciences, Peking University, Beijing 100871, China

Corresponding author

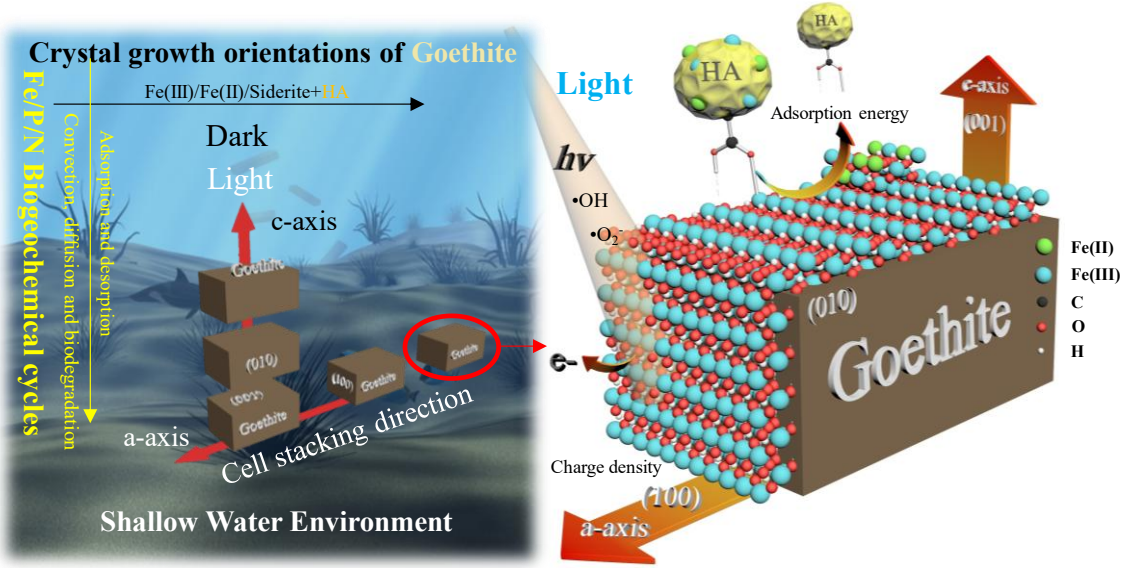
[*] Wenzheng Yu, wzyu@rcees.ac.cn

Abstract

The environmental fate of phosphorus in shallow aquatic systems is closely linked to the properties of iron (oxyhydr)oxide minerals such as goethite, which can bind phosphate and influence its mobility. This study investigates how light exposure during mineral formation affects goethite crystal habit and subsequent phosphate adsorption behavior. Humic-acid (HA)-mediated transformation of siderite or dissolved Fe(II/III) was conducted under simulated shallow-water irradiance (113 $mW \cdot cm^{-2}$) or in dark conditions. We found sunlight-driven changes in the crystal habit of goethite (α-FeOOH) were quantitatively linked to a 33 % reduction in phosphate (P) sequestration capacity compared with dark-formed phases. In the dark, oriented attachment along the c-axis yielded (100)-faceted nanorods (100–500 nm, surface energy 1.22 $J \cdot m^{-2}$) that adsorbed 1.5-fold more P (5 mg $P \cdot L^{-1}$, 24 h) than light-exposed crystals. Light generated $\bullet OH/\bullet O_2^-$ radicals that lowered the electron density of the (100) plane, redirected growth along the a-axis, and produced highly crystalline (001)-terminated rods (1–2 μm). XANES fingerprinting showed that dark phases formed predominantly bidentate Fe–PO_4 complexes (pre-edge intensity 0.25), whereas light phases favored monodentate coordination (pre-edge 0.15). These results suggest that diel irradiation cycles in oxic surface waters may influence goethite reactivity and phosphorus mobility, although extrapolation to natural systems requires consideration of additional environmental complexities.

Keywords: humic acid; light; growth orientation; goethite; adsorption; phosphorus

Synopsis: Prominent role of light in goethite growth along a-axis and the influence of exposed (001)/(100) lattice planes on phosphate complexation.



TOC Art

INTRODUCTION

Fe-bearing minerals are important constituents in soil. They usually exist in the form of nanoparticles, among which the most common minerals are ferrihydrite, goethite, hematite, lepidocrocite, magnetite and schwertmannite, which are spherical, needle, rhomboid, plate, octahedral and "hedge-hog" aggregates, respectively. [1-10] Goethite (α-FeOOH) is the most common Fe(III)-bearing mineral in soils, and it usually acts as a coating attached to other soil mineral surfaces. In addition, it is the final stable form among many iron hydroxides in the natural water environment. [11] Previous studies indicate that the growth orientation of natural goethite in soil appears to occur nearly parallel to the c-axis direction, which may be directly related to the structure of the goethite crystal cell itself, and the nature and concentration of organic matter (OM) in the soil [6, 12]. Despite extensive research on goethite formation in soils, the specific influence of light on crystal growth orientation in shallow aquatic environments remains poorly understood. While soil goethite consistently exhibits c-axis elongation, shallow water minerals experience periodic light exposure that may alter growth pathways. The extent

to which light-driven facet selection occurs under environmental conditions, and its consequences for phosphorus binding, have not been systematically investigated.

Phosphorus (P) and nitrogen (N) compounds in shallow lakes and rivers have basic migration processes such as convection, diffusion and biodegradation under the action of water flow, which are closely related to the Fe-bearing minerals. [13, 14] Most phosphorus and nitrogen entering natural water bodies are adsorbed by suspended Fe-bearing minerals and are transported or deposited with these particles at the bottom of rivers or lakes, forming sediment layers enriched in Fe, P, and N. However, sediments can be resuspended by water flow, potentially releasing significant quantities of these elements back into the water column. Some research studies have pointed out that the migration and transformation of the large majority of elements in the aquatic environment are closely related to the crystallinity, growth orientation, particle size and movement of Fe-bearing minerals. [5, 15-23] Thus, the migration and transformation of Fe, P, and N elements in the aquatic environment cannot be correctly understood and completely described without considering the crystallographic properties of minerals in the water. Although the growth orientation of goethite in soil is predominantly along the c-axis, shallow water environments differ fundamentally from soils in that minerals experience diurnal light-dark cycles and variable light penetration depths. In typical shallow lakes (depth <3 m) with Secchi depths of 0.5-2 m, the light intensity at the sediment-water interface can range from 10-50% of surface irradiance. Our experiments employed fixed irradiance (113.2 $mW \cdot cm^{-2}$) approximating midday summer sunlight; actual field conditions involve diurnal cycles, spectral shifts, and attenuation by dissolved organic matter and suspended particles. Nevertheless, our results suggest the hypothesis that light-driven facet

control could be operative in the upper sediment layers that experience periodic resuspension, though direct field validation is needed. Therefore, it is important to clarify the crystal growth orientation mechanism of minerals in shallow waters for environmental risk assessment, environmental remediation, and as part of the biogeochemical cycle of Fe, P and N elements.

Currently, oriented attachment (OA) [6, 24-27] is widely accepted as a polymerization mode of growth for minerals. [4, 28-40] However, there are still many interrelated factors that remain unknown, particularly those controlling crystal growth, and their influencing mechanisms remain unclear. [25, 26] As the length, width, and height of the mineral unit cell size are generally less than 1 nm, it is very difficult to observe the crystal growth orientation in situ. Hence in previous studies, the focus has been on the stacking mode of a particular lattice plane. [24, 29, 41-50] These studies have great significance for the synthesis and modification of nanomaterials. However, since phosphorus and minerals generally exist in the form of complexes, the main position of action is the surface of minerals. Therefore, the interaction between the mineral and P element in the environment is directly related to the lattice plane characteristics of the exposed surface of the mineral. [51, 52] The selective exposure of the lattice plane is related to the orientation of the mineral stack and growth. The Bravais rule suggests that the most prominent faces of a crystal are those parallel to internal planes having the greatest density of lattice points. [26] As such planes that have the greatest density of lattice points have the lowest surface energy, the crystal is consequently the most stable. Therefore, the first factor to consider in the orientation of crystal growth is the surface energy of each facet. Furthermore, as the degree of unsaturated bonding appears to vary from lattice plane to lattice plane, when the surface atoms are fully relaxed, different charge distributions appear on each lattice plane, producing a

different potential for electron gain and loss; thus, the charge density on the outer surface of the crystal also needs to be considered. Owing to the limitations in the development of characterization technology, many studies have employed density function theory (DFT) calculations to make a more comprehensive assessment of crystal characteristics, such as the crystal surface energy. [16, 19, 26, 33] To clarify the growth orientation of the goethite cell in a shallow water environment, the variation of charge density on the mineral surface under dark and light conditions can be investigated by combining DFT calculations. [53-55]

Another important factor is that OM is ubiquitous in natural water, possessing abundant carboxylic groups (COOH) that facilitate its adsorption onto minerals. Since mineral unit cells are closely wrapped with organic ligands, the adsorption energy between COOH and the lattice plane must be considered. [2, 4, 15, 25, 56-73] In this study, in order to be consistent with environmental conditions, the experiments were undertaken with humic acid (HA), which is a representative component of natural OM that is frequently found in soil, possessing abundant carboxylic groups (COOH). [53, 74, 75] Thus, HA was selected as the representative source of -COOH ligands in order to study the lattice plane selection mechanism of goethite in the shallow water environment. However, when investigating the interfacial reaction, the support of DFT calculations is needed, but the molecular weight of HA is too large and there is no accurate molecular structure for the heterogeneous substance, so an alternative, simpler substance was required to represent -COOH for the calculations. Acetic acid (CH_3COOH) was selected as the representative -COOH ligand for the simulation calculations, as it has a simpler structure and there is no interference from other functional groups. For DFT calculations, acetic acid (CH_3COOH) was selected as a representative model for the carboxylic acid functional groups

in HA. This simplification is justified because: (i) carboxylic groups are the primary functional groups in HA responsible for Fe complexation, (ii) the interaction between Fe oxides and organic matter is dominated by carboxyl-Fe coordination, (iii) the use of a simple molecular model allows rigorous quantum mechanical calculations that would be computationally prohibitive for the full heterogeneous HA structure, and (iv) previous studies have successfully employed similar carboxylic acid models to investigate organic matter-mineral interactions. While we acknowledge that this simplification does not capture the full complexity of HA (e.g., aromatic moieties, variable molecular weight), it provides mechanistically relevant insights into carboxyl-specific binding energetics.

Since Fe(III)/Fe(II) and colloidal iron oxide particles predominate in shallow waters, the growth orientation of mineral transformation products from Fe(III)/Fe(II), induced by HA under light and dark conditions, were investigated. Previous studies have found that iron (hydr)oxides in shallow water, or near the water surface, are vulnerable to light-induced transformations.[7, 37, 72] As the crystals grew and aggregated, most of them were deposited as sediments at the bottom of lakes or rivers, where the effect of light was diminished or even lost. Therefore, in order to simulate the crystallization path of iron-bearing minerals under the influence of light in shallow water as much as possible, a reaction time of 3 hours was chosen. The choice of a 3-hour reaction time was based on several considerations. First, we aimed to capture the initial crystallization pathway before extensive settling and light attenuation occur in natural systems. In shallow water, suspended minerals may be exposed to near-surface irradiance for periods of hours during turbulent mixing or before settling to darker depths. Second, preliminary time-course experiments (0.5-24 h, data not shown) indicated that the

facet-selective growth orientation was established within the first 3 h, with longer times resulting primarily in crystal growth along the already-established orientation rather than changes in facet preference. Third, 3 h is sufficient to observe the transition from amorphous precursors to crystalline goethite while minimizing secondary transformations that might obscure the light effect. We acknowledge that complete transformation of siderite to goethite under natural conditions occurs over much longer timescales (days to years), but the initial facet-selection event that determines the growth trajectory likely occurs during early crystallization.

Based on the considerations above, this study was designed to test the following hypotheses: (1) Light exposure during goethite formation in the presence of HA alters the crystal growth orientation compared to dark conditions, leading to different facet exposures; [31] (2) These light-induced changes in facet exposure result from radical-mediated modifications of surface charge density that favor growth on specific lattice planes; (3) The exposed facet type (100 vs. 001) influences phosphate adsorption capacity and coordination geometry; and (4) These processes, observed under controlled laboratory conditions, have potential implications for phosphorus cycling in shallow aquatic environments where minerals experience diurnal light-dark cycles.

MATERIALS AND METHODS

Materials. The siderite was prepared by mixing solutions of ferrous sulfate ($FeSO_4 \cdot 7H_2O$) and anhydrous sodium bicarbonate (Na_2CO_3), and autoclaving at 130 °C, according to methods that have been previously published. [75] The detailed method is described in the Supplementary Information (Section S1, SI).

Sample Analysis and Data Evaluation. The crystal facet exposure and growth orientation of goethite were determined using a combination of techniques: (i) High-resolution TEM (HRTEM) lattice fringe measurements provided direct visualization of crystallographic planes, with interplanar spacings matched to goethite reference patterns (ICDD 29-0713) to identify specific facets; (ii) Fast Fourier Transform (FFT) analysis of HRTEM images confirmed the crystallographic orientation by generating diffraction patterns corresponding to specific zone axes; (iii) Selected area electron diffraction (SAED) provided additional confirmation of crystal orientation; (iv) The angle between visible crystal edges and measured lattice fringes was used to determine growth direction relative to crystallographic axes; and (v) DFT-calculated surface energies and charge densities provided theoretical predictions of facet stability that were compared with experimental observations.

Throughout this manuscript, we use the notation 'Dark-Goe(100)' to refer to goethite formed under dark conditions that exhibits predominant (100) facet exposure, and 'Light-Goe(001)' for goethite formed under light with predominant (001) facet exposure. This nomenclature reflects the dominant crystal facet exposed to the environment as determined by HRTEM and DFT analysis. First-principles calculations were performed by using the Vienna Abinitio Simulation Package (VASP), [76-79] and the detailed methods of the DFT calculations [16, 19, 26, 33] are given in the Supplementary Information (Section S2, SI). We calculated the pristine goethite surface energy of the lattice planes. The Bravais rule [26] suggests that the surface energy of (010) lattice planes is the lowest, and therefore it is difficult for the crystal to grow perpendicularly on this surface. In consequence, the (010) lattice plane is not an ideal contact location for OA and the competition is mainly between (100) and (001) facets. The surface energy values reported in

192 this study were calculated using first-principles DFT calculations as described in Section S2 of
193 the Supplementary Information. For the pristine FeOOH surfaces, we obtained surface energies
194 of 1.22 $J \cdot m^{-2}$ for the (100) facet and 1.13 $J \cdot m^{-2}$ for the (001) facet (Table S1).
195 X-ray diffractometry (XRD, X'Pert PRO MPD, PANalytical, Netherlands), Field emission
196 scanning electron microscopy (SEM, SU-8020, HITACHI, Japan), Field emission transmission
197 electron microscopy (TEM, JEM-2100F, JEOL, Japan), X-ray photoelectron spectroscopy
198 (XPS, PHI Quantera II, ULVAC, Japan), and three-dimensional fluorescence excitation-
199 emission matrix spectrometry (3D-EEM, F-4600, HITACHI, Japan) were used to analyze the
200 phase composition of the samples. Specific surface areas of selected samples were determined
201 by N_2 adsorption-desorption isotherms at 77 K using a Quadrasorb SI-MP surface area analyzer
202 (Quantachrome, USA). Samples were degassed at 105°C for 12 h prior to analysis, and surface
203 areas were calculated using the Brunauer-Emmett-Teller (BET) method over the relative
204 pressure range P/P_0 = 0.05-0.30. Electron spin resonance spectrometer (ESR, A300, Bruker,
205 Germany) was utilized with DMPO as a radical capture agent to detect the super oxygen radical
206 and hydroxyl radical. The detailed methods are given in the Supplementary Information
207 (Section S3, SI).
208
209 **Batch experiments.** The transformation process of Fe(III)/Fe(II)/Siderite induced by humic
210 acid (HA: CAS: 68131-04-4; 0~10 mg/L) under dark (Fe(III)/Fe(II): 0.5 mg/L; Siderite: 0.5
211 g/L; denoted as Fe(III)HD_{3h}-0.5, Fe(II)HD_{3h}-0.5, and SHD_{3h}, respectively) and light (Fe(III):
212 0.5 mg/L; denoted as Fe(III)HL_{3h}-0.5, Fe(II)HL_{3h}-0.5, and SHL_{3h}, respectively) conditions for
213 3 h, and the growth characteristics of goethite crystal, were investigated. In light-dark cycle

214 experiments, the transformation process of siderite induced by humic acid under light for 3 h
215 (1 h) and then dark for 0.5 h (denoted as SHL_{3h} $D_{0.5h}$ and SHL_{1h} $D_{0.5h}$), successively, were
216 investigated.
217 Each reaction solution contained 0.5 mg/L sodium bicarbonate ($NaHCO_3$) to provide a
218 consistent background electrolyte and pH buffer capacity. The reaction pH was maintained at
219 approximately 7.0 throughout the experiments by continuous monitoring and adjustment. No
220 chemical buffer was used to avoid potential interference with crystal growth. Instead, pH was
221 monitored at 30-min intervals using a calibrated pH meter (Mettler Toledo FE20), and when
222 deviations exceeded ±0.2 pH units, the pH was carefully adjusted using 0.01 M HCl or NaOH
223 as needed. Over the 3-h reaction period, pH remained within 6.8-7.2 for all experiments, with
224 no adjustment required for most samples. Solution ionic strength was not adjusted beyond the
225 $NaHCO_3$ contribution (approximately 0.01 mM), which is representative of freshwaters with
226 low to moderate ionic strength. All solutions were prepared using ultrapure water (18.2 MΩ·cm,
227 Milli-Q) to minimize contamination. Dissolved oxygen (DO) concentration was monitored
228 throughout all experiments using a calibrated optical DO probe (Hach LDO, USA). Initial DO
229 was 4.0 ± 0.2 mg/L for all experiments, achieved by equilibrating solutions with ambient air.
230 Final DO concentrations after 3 h reaction were measured for each experimental condition and
231 are reported in figure captions (Figures 1-6). The concentrations of total Fe and Fe(II) were
232 determined by Inductively Coupled Plasma Spectroscopy (Optima 8300, Perkinelmer, USA)
233 and UV-visible absorbance spectrophotometer at 510 nm (UV-2600, Shimadzu, Japan, by the
234 phenanthroline method), respectively. All adsorption experiments were conducted in triplicate
235 (n=3) using separate batches. Results are presented as mean values with standard deviations

shown as error bars in Figure 2h. A xenon lamp (CEL-PE300E-3A, China; 10-500 $mW \cdot cm^{-2}$, full spectrum: 200-1100 nm) was used as the light source in the experiment. The current of the xenon lamp was adjusted to 14.5 A, the distance between the reaction liquid in the reaction bottle and the xenon lamp was 4.5 cm, and the optical power density in the reaction center was 113.2 $mW \cdot cm^{-2}$, which was approximately equal to the intensity of the sun at ground level. The reaction bottles were mixed by placing them on a magnetic stirrer with a temperature controller (continuous cooling water around the reaction bottle was used to control the temperature of the reaction solution at 298 k, excluding the effect of reaction temperature on crystal growth) at a stirring rate of 100 rpm. After aging for a set time (0.5 h, 1 h, and 3 h), the precipitate was freeze-dried for 12 h, and after collection used for adsorption kinetics studies and XANES experiments. These time points were selected to capture the early stages of crystal nucleation and growth before extensive crystal maturation. The 0.5 h time point allowed observation of initial amorphous precursor formation, 1 h captured the transition to crystalline phases, and 3 h provided sufficient crystalline material for facet characterization while still reflecting the initial growth orientation established under light or dark conditions. Adsorption kinetics studies were conducted with different incubation times from 1 h to 48 h. Batch adsorption experiments were carried out with an initial phosphate concentration of 5 mg/L as P (0.16 mmol/L KH_2PO_4) at 298 K. The suspensions were agitated on an orbital shaker at 150 rpm, and aliquots were collected at predetermined time intervals (1, 3, 12, 24 and 48 h) for phosphate analysis by the molybdenum blue method. The P K-edge XANES measurements were taken at the beamline 4B7A at the Beijing Synchrotron Radiation Facility (BSRF, Beijing, China).

RESULTS AND DISCUSSION

Controlling factors and potential environmental risks of goethite growth direction in shallow water environments.

For readers unfamiliar with goethite crystallography, it is helpful to note that goethite (α-FeOOH) crystallizes in the orthorhombic system (space group Pnma) with unit cell parameters a = 9.91 Å, b = 3.01 Å, and c = 4.58 Å. The crystallographic axes correspond to different structural directions: the c-axis runs parallel to the double chains of $FeO_3(OH)_3$ octahedra, the a-axis is perpendicular to these chains, and the b-axis is the shortest axis connecting octahedral chains. Growth along the c-axis produces elongation in the direction of the octahedral chains, while growth along the a-axis produces elongation perpendicular to them. Under the dark conditions (Figures 1: a to f), large amounts of rod-like substances with a length of approximately 100-500 nm were observed by SEM (Figure 1a) and TEM (Figures 1b and 1d) in the sample of Fe(III)HD_{3h}-0.5. The resolved interplanar spacings along the rod-like substances were 2.64 Å (Figure 1c), which corresponded to the (301) lattice planes of goethite (inset of Figure 1c). All the resolved interplanar spacings (Figures 1e and 1f, HRTEM) ranged from 3.27 Å to 3.41 Å, which corresponded to the (201) lattice planes of goethite (inset of Figures 1e and 1f). The angle between the long axis of the nanorods and these lattice fringes (approximately 90°) indicates that the elongation direction is parallel to [001]. Second, DFT calculations (Figure 1h, i) demonstrate that -COOH ligands preferentially bind to the (001) facet, providing a mechanistic basis for c-axis growth.

In order to identify the lattice plane selection mechanism during the process of crystal growth, we calculated the pristine goethite charge density, adsorption energy and ligand binding

280 configurations of the lattice planes using DFT (see Section S2 of Supporting Information for
281 calculation formulas and analytical methods). The functional group, -COOH, has been shown
282 by a large number of studies [12, 80] that it can chelate with Fe(III) and generate adsorption energy
283 with goethite, which may change the growth direction of goethite. As the molecular weight of
284 HA was too large, acetic acid (CH_3COOH) was used as the representative -COOH ligand for
285 the simulation calculation. The possible ligand binding configurations (top, bridge, and hollow)
286 as initial states for simulation were considered. The configurations of CH_3COOH on the (001)
287 facet of goethite are shown in Figure 1g. It was found that the bridge and hollow configurations
288 eventually transformed to the top configuration (Figures S1: a to c, SI) after relaxation, and the
289 adsorption energy of a single CH_3COOH group was calculated to be -1.24 eV for (001) facets
290 (Table S1, SI). In comparison, for the (100) facet, the adsorption energy was all positive,
291 showing relatively poor adsorption activity (Figures S1: d to f and Table S1, SI). Moreover, the
292 difference in the charge density implied that electrons in the CH_3COOH on the (001) and (100)
293 facets were transferred to their contact positions after the adsorption (Figures 1h and 1i).
294 Compared to the atoms inside the unit cell, it was calculated that the iron atom on the (001)
295 facet of pristine FeOOH accumulated 0.21-0.30 electrons from the Bader charge analysis. After
296 adsorption, the iron atom lost nearly 0.1 electrons, which interacted strongly with adsorbed
297 CH_3COOH, and maintained a higher valence state, and tended to be stable. However, the initial
298 valence state of the iron atom on the (100) facet was slightly higher, and Bader showed that
299 only 0.04 electrons were gathered compared with inside the unit cell, so the surface iron atom
300 maintained a stable state similar to the internal one. After the adsorption of CH_3COOH, the
301 surface iron atom lost nearly 0.07 electrons and reached, or even exceeded, the valence state of

the inside iron atom, which was also the reason for the positive adsorption energy on the (100) facet. The results of DFT suggest that the -COOH ligand can bring free iron atoms onto the (001) facet by chelation and induce goethite to grow vertically on this surface, which is consistent with the results of the HA-induced experiment in dark conditions (Figures 1a to 1f). Hence, the results indicate that the adsorption energy of the -COOH ligand at the different lattice planes plays a key role in controlling self-orientation during OA. This may be one of the important reasons to explain the growth orientation of natural goethite in soil (no light), which was parallel to the c-axis.

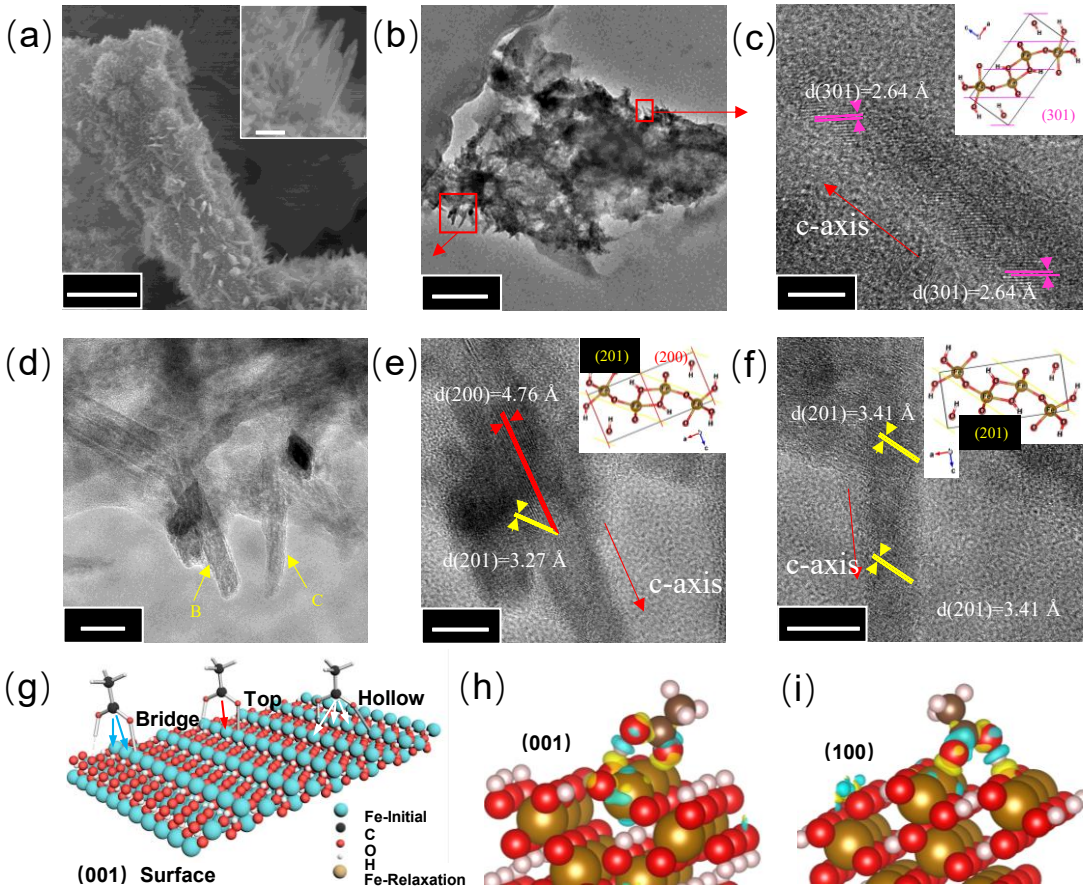


Figure 1. The crystallization path of Fe(III) induced by HA under dark conditions. The representative SEM (**a**), TEM (**b**), and HRTEM (**c**, **d**, **e**, and **f**) images of the crystal products of Fe(III) (0.5 mg/L) induced by HA for 3 h under dark conditions (Fe(III)HD_{3h} -0.5). Schematic diagrams of the goethite unit cell structure ([space group *Pnma*] with lattice constants a = 9.91 Å, b = 3.01 Å and c = 4.58 Å, inset of Supplementary Figure 1c, 1e, and 1f), were drawn by VESTA software (National Museum of Nature and Science, Japan). (**g**) The possible ligand binding configurations of CH_3COOH on the (001) facet of goethite. Top

configuration (Fe atom directly coordinated, red arrow), bridge configuration (coordinated between two Fe atoms, blue arrow), and hollow configuration (coordinated in three-fold site, green arrow). After relaxation, bridge and hollow configurations converged to the top configuration (see Figure S1). (**h**) The difference of charge density of FeOOH (001) facet with adsorbed CH_3COOH. (**i**) The difference of charge density of FeOOH (100) facet with adsorbed CH_3COOH. The level of the iso-surface is 0.003 e/Å. The electron excess and deficiency are demonstrated as yellow and blue iso-surfaces, respectively. The initial concentration of Fe(III) was 0.5 mg/L, the initial concentration of $NaHCO_3$ was 0.5 mg/L, and the initial concentration of HA was 2 mg/L (T=298 K, pH 7). The initial concentration of dissolved oxygen (DO) was 4 mg/L, and the final concentration of DO was 4 mg/L. Samples were freeze-dried for 12 h. Scale bars: **a**: 1 μm, inset 100 nm; **b**: 200 nm; **c**: 5 nm; **d**: 20 nm; **e** and **f**: 10 nm.

In addition, under the light conditions (Figures 2: a to c), large amounts of rod-like substances with a length of approximately 1-2 μm were observed by SEM (Figure 2a) and TEM (Figure 2b) in the sample of Fe(III)HL_{3h}-0.5, which were significantly larger than the rod-like goethite under dark conditions (approximately 100-500 nm in the sample of Fe(III)HD_{3h}-0.5; Figures 1a, 1b and 1d). The resolved interplanar spacings along the rod-like substance were 2.34 Å (Figure 2c), which corresponded to the (002) lattice planes of goethite (inset of Figure 2c). The results revealed that the rod-like substance was goethite, and it was induced by HA to grow along the a-axis. The observation that light promotes goethite growth along the a-axis is consistent across all three experimental systems investigated. For Fe(III)-derived goethite (Figure 2), HRTEM showed (002) lattice fringes (2.34 Å) perpendicular to the elongation direction, indicating a-axis growth. For Fe(II)-derived goethite under light (Figure 3f-j), similar (002) fringes (2.26 Å) were observed. For siderite-derived goethite under light (Figure 5e-f), the dominant lattice fringes were also consistent with a-axis growth. This consistency across different Fe sources (Fe(III), Fe(II), and siderite) suggests that the light-driven facet selection mechanism is robust and not dependent on the specific Fe precursor.

343 The growth direction of goethite under light conditions was different from that under dark
344 conditions, so we also conducted DFT calculations to analyze its growth orientation mechanism,
345 and the lattice planes charge density of goethite using DFT are shown in Figures 2d to 2g. The
346 DFT results suggested that the atomic coordination saturation on the initial lattice planes (001)
347 and (100) were different, which results in a different charge density on the two surfaces. The
348 (001) and (100) facets' charge density of pristine FeOOH are shown in Figures 2d and 2f,
349 respectively. When the lattice planes were fully relaxed, the charge density around the iron
350 atom of the (001) facet had clearly accumulated (Figure 2e), showing a strong ability to acquire
351 electrons. However, the (100) facet was the opposite, with a lower charge density and a poor
352 electron acquisition ability (Figure 2g), which is related to the degree of unsaturation of the
353 octahedral structure of iron atoms on the surfaces. Therefore, under light conditions the
354 irradiation energy (*hv*) and newly generated free radicals appeared to act more readily on the
355 (001) facet of goethite, thereby changing the charge density, making the goethite grow more
356 easily and accumulate towards the a-axis of goethite.

357 The amount and complex form of phosphate adsorption by goethite in different growth
358 directions were different (Figures 2h and 2i). The above experimental analysis suggested that
359 goethite grew along the c-axis in the dark environment, and the (100) facet was exposed to the
360 environment, denoted as Dark-Goe(100); the sample under light conditions was denoted as
361 Light-Goe(001). The adsorption capacity of both samples increased rapidly in the initial stage,
362 followed by a small further enhancement of phosphate removal, and then equilibrium was
363 reached after 24 h (Figure 2h). The adsorption capacity of Dark-Goe(100) was 1.5 times that
364 of Light-Goe(001). The above DFT analysis suggested that the surface energy of the (100) facet

was 1.22 $J \cdot m^{-2}$, which was slightly greater than that of the (001) facet (1.13 $J \cdot m^{-2}$), so the (100) facet adsorbed more phosphate to eliminate the excessive surface energy. Another contributing factor may be the difference in crystallinity: Light-Goe(001) exhibits higher crystallinity than Dark-Goe(100), while less crystalline materials such as Dark-Goe(100) tend to be more porous with adsorption sites that are not all equally accessible. This difference in site accessibility, previously documented for iron (oxyhydr)oxides,[9, 23, 36] can influence both the capacity and kinetics of phosphate adsorption. The pseudo-second-order model fit (R^2 = 0.999 for Dark-Goe(100) vs. 0.945 for Light-Goe(001)) is consistent with more heterogeneous site accessibility in the less crystalline material.

The overall spectra of XANES (Figure 2i) show that there are differences in both the whiteline (strongest peak) energies and pre-edge peak intensities. Nidhi Khare et al. found that the pre-edge feature occurring between 2150 and 2154 eV became more intense with increasing Fe/P ratio, and no spectral pre-edge occurred in the absence of Fe(III), where Fe/P = 0.[51] They also found that with increasing Fe/P ratio, the aqueous Fe(III)–PO_4 solutions increased in the degree of bidentate relative to monodentate bonding. [51] To provide quantitative comparison of the XANES spectra, we analyzed the pre-edge feature intensities by fitting Gaussian peaks after subtracting a linear background. Dark-Goe(100) exhibited a pre-edge peak at 2152.3 eV with integrated intensity of 0.25 ± 0.02 (arbitrary units), while Light-Goe(001) showed a pre-edge peak at 2152.1 eV with integrated intensity of 0.15 ± 0.02. Following the calibration approach of Khare et al.,[51] the pre-edge feature intensity of Dark-Goe(100) was closer to the phosphate adsorption intensity of ferrihydrite (Figure 2i), which was more inclined to bidentate-bonded Fe–PO_4 complexes (pre-edge intensity 0.25). However, the pre-edge feature

intensity of Light-Goe(001) was relatively weak, which was more inclined to monodentate-bonded Fe–PO_4 complexes (pre-edge 0.15). The pseudo-second-order adsorption models (Figure 2h) and XANES (Figure 2i) results suggested that the (100) facet exposed to the surface of goethite grown under dark reaction conditions, which, due to the high surface energy (1.22 $J \cdot m^{-2}$) and poor crystallinity, had a stronger adsorption of phosphate than in light conditions, and the complexation form was more similar to bidentate-bonded Fe–PO_4 complexes, suggesting a shift in phosphate coordination mode with facet exposure.

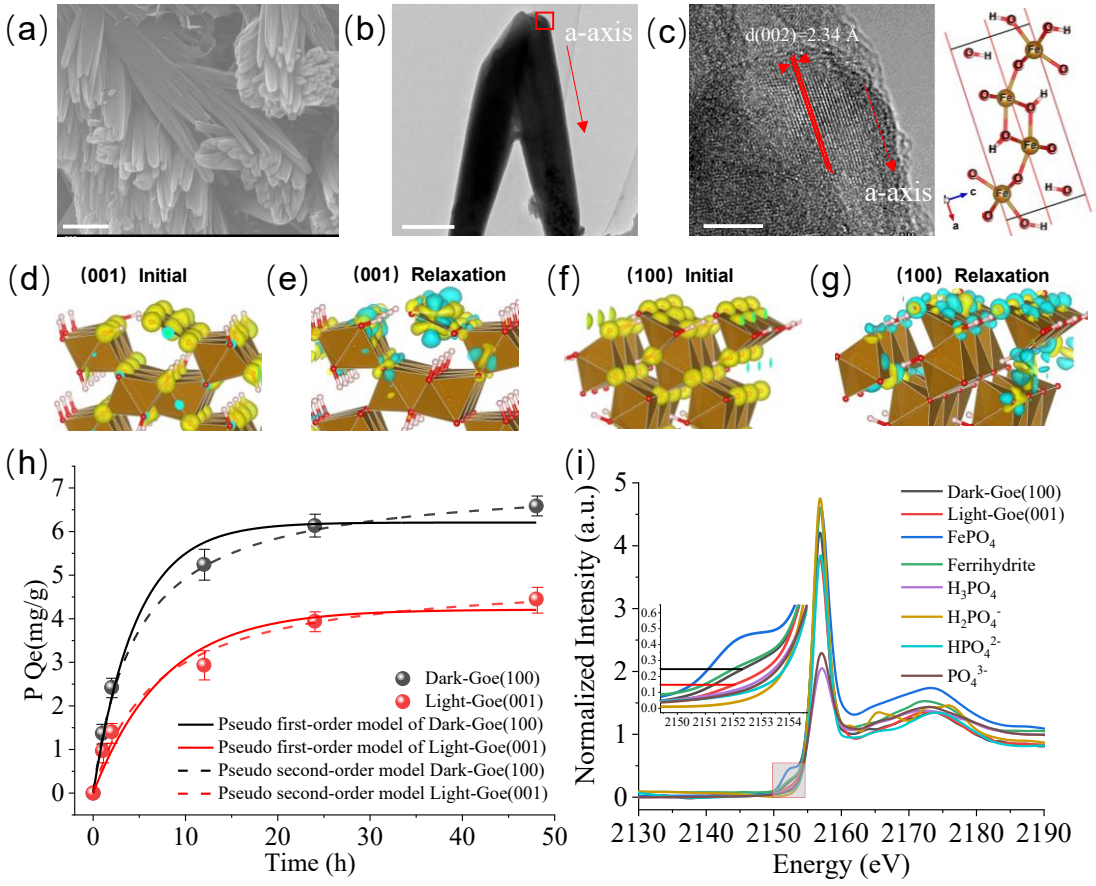


Figure 2. The crystallization path of Fe(III) induced by HA under light conditions. The representative SEM (**a**), TEM (**b**), and HRTEM (**c**) images of the crystal products of Fe(III) (0.5 mg/L) induced by HA for 3 h under light conditions (Fe(III)HL_{3h}-0.5). Schematic diagrams of the goethite unit cell structure ([space group *Pnma*] with lattice constants a = 9.91 Å, b = 3.01 Å and c = 4.58 Å, inset of Figure 2c), were drawn by VESTA software (National Museum of Nature and Science, Japan). (**d**) The initial (001) facets charge density of FeOOH. (**e**) The (001) facets charge density of pristine FeOOH after full relaxation. (**f**) The initial (100) facets charge density of FeOOH. (**g**) The (100) facets charge density of pristine FeOOH after full

relaxation. The level of the iso-surface is 0.003 e/Å. (**h**) Kinetic adsorption curve of Dark-Goe(100) and Light-Goe(001). Data points represent mean values from triplicate experiments (n=3) and error bars indicate standard deviation. Adsorption conditions: initial P concentration 5 mg/L, pH 7, T = 298 K, solid concentration 0.5 g/L. (**i**) Normalized P K-edge XANES spectra for Dark-Goe(100) and Light-Goe(001). The initial concentration of Fe(III) was 0.5 mg/L, the initial concentration of $NaHCO_3$ was 0.5 mg/L, and the initial concentration of HA was 2 mg/L (T=298 K, pH 7). The initial concentration of DO was 4 mg/L and the final concentration of DO was 3.5 mg/L. Samples were freeze-dried for 12 h. Scale bars: **a**, and **b**: 500 nm; **c**: 5 nm.

In conclusion, the calculation results of DFT suggest that light induces the growth of goethite along the a-axis, by changing the charge density of the (100) lattice plane, while COOH ligands induce the growth of goethite along the c-axis due to its binding energy on the (001) lattice plane of goethite. Light has a prominent role in the direction of goethite growth, when light and HA both act on the goethite. At the same time, different crystal planes exposed to the outer surface of goethite have different influences on the migration and transformation of environmental pollutants, which will be further discussed in the subsequent 'Environmental Implications' section.

The differing effects of Fe(II) and Fe(III) on goethite growth orientation.

Under dark conditions (Figure 3: a to e), large amounts of leaf-like substances with a size of approximately 300-400 nm were observed by SEM (Figure 3a) and TEM (Figure 3b) in the sample of Fe(II)HD_{3h}-0.5. The resolved interplanar spacings along the rod-like substance were 2.49 Å, and the other resolved interplanar spacings of some scattered areas ranged from 1.51 Å to 1.55 Å (Figure 3c, HRTEM), which corresponded to the (400) and (601) lattice planes of goethite (inset of Figure 3c), respectively. The results revealed that the leaf-like substance was goethite, and its distinct crystal band grew in the c-axis direction. The interior (A in Figures 3d and 3e) and surface (B in Figures 3d and 3e) of Fe(II)HD_{3h}-0.5 were compared by XPS, and

the results suggested that the main component of the Fe(II)HD_{3h}-0.5 interior was still ferrous iron, and a small amount of goethite (A in Figures 3d and 3e). However, the binding energy of goethite on the surface of Fe(II)HD_{3h}-0.5 was obviously enhanced (B in Figures 3d and 3e), which suggested that Fe(II) was first agglomerated and gradually oxidized and crystallized. The 3D-EEM spectra (Figure S2) show the evolution of HA fluorescence over time. At t = 0 min (Figure S2a), the characteristic humic-like fluorescence peaks (Ex/Em: 250/450 nm and 350/450 nm) are clearly visible. Within 2-5 min (Figure S2b, c), fluorescence intensity decreases substantially, suggesting complexation of HA with Fe(II) that quenches fluorescence. After 20-40 min (Figure S2e, f), fluorescence intensity begins to recover, and by 90-120 min (Figure S2g, h), fluorescence approaches the initial intensity. This fluorescence recovery is consistent with release of HA as Fe(II) is oxidized and incorporated into crystalline goethite, consistent with previous reports of organic matter release during iron oxide crystallization.[37, 39, 72] This experimental result does not prove that Fe(II) can induce the growth of goethite along the c-axis (interference of HA), but the presence of Fe(II) causes goethite to form leaf-like structures along both the a-axis and the c-axis (Figure 3c). Hence the Fe(II) plays a key role in controlling self-orientation during agglomeration, which will be discussed further below.

In addition, under light conditions (Figure 3: f to j), similar to the above phenomenon, large amounts of rod-like substances with a length of approximately 1-2 μm were observed by SEM (Figure 3f) and TEM (Figure 3g) in the sample of Fe(II)HL_{3h}-0.5. The resolved interplanar spacings along the rod-like substance were 2.26 Å (Figure 3h), which corresponded to the (002) lattice planes of goethite (inset of Figure 3h). The results revealed that the rod-like goethite was induced by HA to grow along the a-axis. However, some leaf-like substances next to rod-

like goethite with a size of approximately 200-300 nm were observed by SEM (Figure 3f) and TEM (Figure 3i). The calculated lattice planes (d(400)=2.43 Å and d(002)=2.23 Å, Figure 3j) and the angle between them revealed that the leaf-like substance was goethite, whose growth direction was perpendicular to the crystallographic b-axis of goethite.

Fe(II) may play a key role in controlling self-orientation during OA: the crystal band along the c-axis of goethite was formed first, and then the agglomerated Fe ions near the crystal band gradually rearranged and crystallized toward the a-axis of goethite. Light, though not completely dominant, tends to induce more goethite growth toward the a-axis, when light, Fe(II) and HA all act on the goethite.

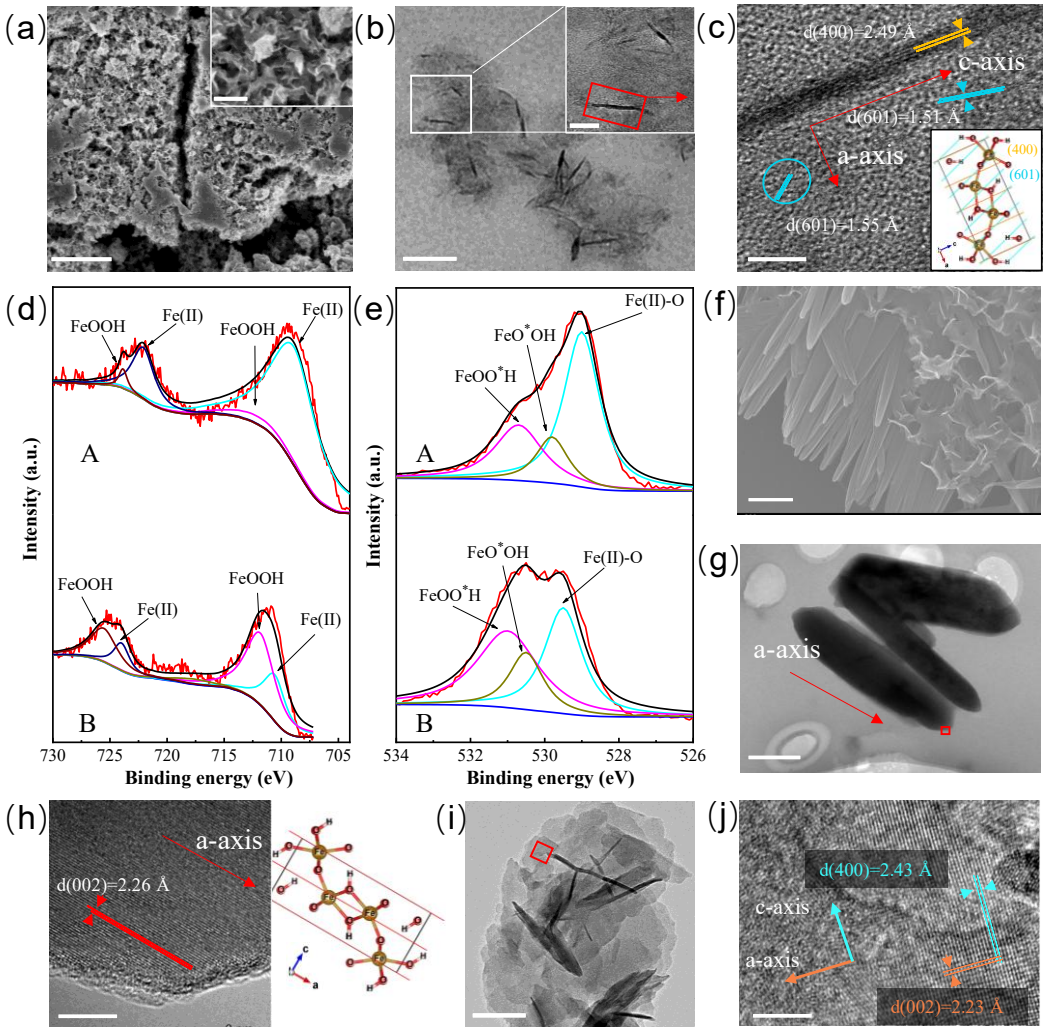


Figure 3. The crystallization path of Fe(II) induced by HA under dark conditions. The representative

SEM (**a**), TEM (**b**), and HRTEM (**c**) images of the crystal products of Fe(II) (0.5 mg/L) induced by HA for 3 h under dark conditions (Fe(II)HD_{3h}-0.5). High-resolution XPS spectra of Fe 2p (**d**) and O 1s (**e**) of Fe(II)HD_{3h}-0.5 (inside 20 nm: A, outside: B). The representative SEM (**f**), TEM (**g** and **i**), and HRTEM (**h** and **j**) images of the crystal products of Fe(II) (0.5 mg/L) induced by HA for 3 h under light conditions (Fe(II)HL_{3h} -0.5). Schematic diagrams of the goethite unit cell structure ([space group *Pnma*] with lattice constants a = 9.91 Å, b = 3.01 Å and c = 4.58 Å, inset of Figure 3**c** and 3**h**), were drawn by VESTA software (National Museum of Nature and Science, Japan). The initial concentration of Fe(II) was 0.5 mg/L, the initial concentration of $NaHCO_3$ was 0.5 mg/L, and the initial concentration of HA was 2 mg/L (T=298 K, pH 7). The initial concentration of DO was 4 mg/L and the final concentration of DO was 3.7 mg/L (Fe(II)HD_{3h}-0.5) and 3.6 mg/L (Fe(II)HL_{3h} -0.5). Samples were freeze-dried for 12 h. Scale bars: **a**: 2 μm, inset 300 nm; **b** and **i**: 100 nm, inset 20 nm; **c**, **h** and **j**: 5 nm; **f**, and **g**: 500 nm.

Effect of light on the crystallization and oxidation path of dissolved Fe(II) (Siderite) induced by humic acid. In the siderite mineral transformation process under dark conditions for 3 h and 1 h (Figure 4), a large quantity of nanometer-sized particles (grain sizes ranging from 50 to 60 nm, Figure 4a) was observed on the surface of siderite (inset of Figure 4a). The SHD_{3h} retained the size of the original siderite sphere, but an obvious phase difference occurred on its surface (Figures 4a and 4b). It was surrounded by a large amount of rod-like and plate-like substances (plate sizes range from 100 to 300 nm; Figure 4b), which was similar to the surface of SHD_{1h} (Figure 4c). The main XRD diffraction peaks of siderite (spectra A in Figure S3a, SI) and SHD_{3h} (spectra C in Figure S3a, SI), located at 2θ = 24.5°, 32°, 38°, 42°, 46°, 51°, 52.5°, 61.5° were ascribed to siderite (ICDD (29-0696)); there were other diffraction peaks located at 2θ = 17.8°, 21.2°, 33.2°, 34.6°, and 36.6° (spectra C in Figure S3a, SI), which corresponded to goethite (ICDD (29-0713)). The XRD results reveal that the intensity of the diffraction peaks of siderite decreased and that new diffraction peaks of goethite appeared in the SHD_{3h} sample. The Fe 2p peaks, which were assigned to $FeCO_3$, displayed broad Fe 2p3/2 and Fe 2p1/2 lines located at 710.7 ± 0.2 eV and 724.9 ± 0.2 eV, respectively. [75] The peak at

712.6 ± 0.2 eV was assigned to the formation of goethite (B in Figure S3b, SI). [81, 82] Furthermore, the detailed O 1s XPS spectra of the SHD_{3h} are shown in Figure S3c, which was assigned to $FeCO_3$ located at 529.5 ± 0.2 eV. The peaks of FeO*OH and FeOO*H (the * symbol, located in the upper right of the identifying atom, represents the binding energy between the atom and other atoms and is used to distinguish multiple atoms of the same element in the one functional group) were located at 530.4 ± 0.2 eV and 531.9 ± 0.2 eV, respectively. The O 1s peak located at 531.3 ± 0.2 eV was assigned to ferrihydrite, while the peak at 533.1 ± 0.2 eV was attributed to CO*OH in HA.[83] The XPS results are consistent with the above XRD analysis. It is noted that a large quantity of spherical substances (diameter sizes range from 20 to 30 nm; Figure 4c) was beneath the surface of this new coating (goethite). These spherical substances were also different from the surface appearance of siderite (Figure 4a). It suggested that these might be a precursor of goethite (ferrihydrite, XPS in Figure S3c).

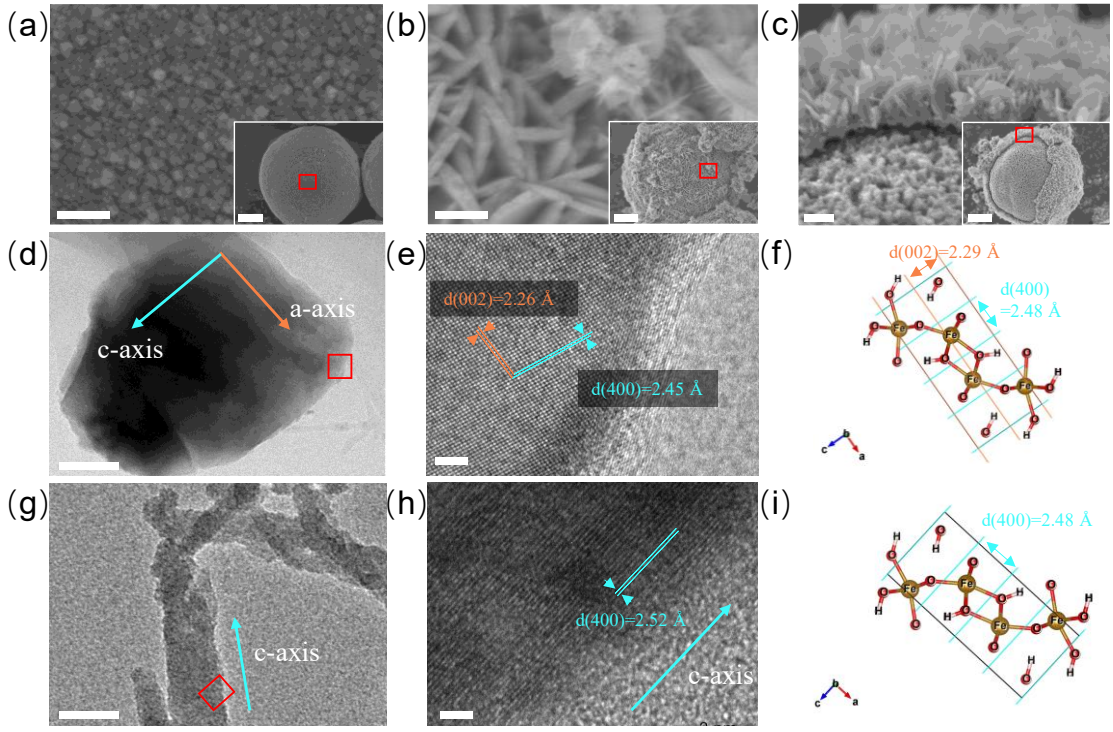


Figure 4. The growth orientation of siderite mineral transformation products induced by humic acid under dark conditions. Representative SEM images of siderite (**a**), SHD_{3h} (**b**), and SHD_{1h} (**c**). The

503 representative TEM and HRTEM images of the plate-like (**d** and **e**) and rod-like (**g** and **h**) substances of
504 SHD_{3h}. The schematic diagrams of the goethite ([space group *Pnma*] with lattice constants a = 9.91 Å, b =
505 3.01 Å and c = 4.58 Å) unit cell structures (**f** and **i**) were the corresponding regions in (**e**) and (**h**), which
506 were drawn by VESTA software (National Museum of Nature and Science, Japan). The initial concentration
507 of siderite was 0.5 g/L, and the initial concentration of HA was 2 mg/L (T=298 K, pH 7). The xenon light
508 intensity was 113.2 $mW \cdot cm^{-2}$. The initial concentration of dissolved oxygen (DO) was 4 mg/L. The final
509 concentration of DO was 3.3 mg/L. Samples were freeze-dried for 12 h. Scale bars: **a**, **b**, and **c**: 200 nm,
510 inset 2 μm; **d** and **g**: 50 nm; **e** and **h**: 2 nm.

511

512 The plate-like (SHD_{3h}, Figure 4d) and rod-like (SHD_{3h}, Figure 4g) substances were
513 analyzed by TEM. The calculated lattice planes (d(400)=2.45 Å and d(002)=2.26 Å, Figure 4e)
514 and the angle between them revealed that the plate-like substance was goethite, whose growth
515 direction was along the crystallography a-axis and c-axis, respectively. The lattice
516 measurement results of the goethite crystal cell (Figure 4f) were consistent with the above
517 results. The calculated lattice planes (d(400)=2.52 Å, Figure 4h) revealed that the rod-like
518 substance also was goethite, and its growth direction was along the crystallography c-axis,
519 which was consistent with the lattice measurement results of the goethite crystal cell (Figure
520 4i).

521 Previous research [55, 75] has revealed that the possible effects of Fe(II) on mineral growth
522 need to be taken into account. The concentration of Fe(II) and the total Fe of the filtrates
523 (siderite after reacting with HA (2 mg/L) under dark) were measured (Figure S4a, SI), which
524 were approximately 0.29 mg/L and 0.52 mg/L, respectively. The results reveal that the
525 abundant carboxyl groups of HA may chelate Fe from the surface of siderite ($FeCO_3$) , [75] which
526 can also induce agglomerations of Fe(III) and control self-orientation to assemble along the c-
527 axis of goethite independently.

528 In addition, under the light conditions (Figure 5), the size of the SHL_{3h} sample was larger

than that of the initial siderite sphere (Figure 5a), and its surface changed significantly (Figures 5b). A large quantity of nanometer-sized particles (grain sizes range from 50 to 200 nm; Figure 5b) was observed on the surface of SHL_{3h}. A large quantity of micron-sized rod-like substances (grain sizes range from 0.6 to 0.8 μm; Figure 5c) was observed on the surface of SHL_{1h}. The results suggested that the morphology of siderite mineral transformation products induced by humic acid under light conditions was rod-like, which was further investigated by TEM (SHL_{3h}, Figure 5d). Two regions of the rod-like substances were observed by high-resolution TEM images (Figures 5e and 5f). The calculated lattice planes (d(301)=2.67 Å and d(002)=2.26 Å, Figure 5e) and the angle between them demonstrated that its major phase was goethite ([space group *Pnma*] with lattice constants a = 9.91 Å, b = 3.01 Å and c = 4.58 Å), which was consistent with the schematic of the goethite unit cell structure (the inset of Figure 5e). The lattice calculation results of another region of the rod-like substance (Figure 5f) agreed with the above analysis results. By comparing HRTEM and the crystal cell parameters of goethite, it was found that the newly generated goethite induced by humic acid under light conditions grew along its a-axis.

Similarly, to assess the induced effect of Fe(II)/Fe(III), the concentration of Fe(II) and the total Fe of the filtrates (siderite after reacting with HA (0 and 2 mg/L) under light) were measured (Figures S4b and S4c, SI). The results revealed that the concentration of Fe(II) and total Fe were 0.37 mg/L and 0.86 mg/L, respectively (Figure S4c, SI). Therefore, we added Fe(II)/Fe(III) at two concentrations (0.5 mg/L and 100 mg/L, respectively) to the transformation experiment of siderite under the conditions of light without HA. (Figure S5, SI). These results demonstrate that, in the absence of HA, neither low concentrations of

Fe(II)/Fe(III) (0.5 mg/L) nor light exposure alone was sufficient to induce formation of crystalline goethite products. Crystallization required the combined presence of HA together with either Fe ions or light, or both. A detailed analysis of the growth orientation of goethite formed from siderite under light with HA is provided in Section S4 of the Supplementary Information, with supporting data shown in Figure S5. In addition, a detailed analysis of the nucleation and growth of goethite induced by light and HA is shown in the SI (Section S6, SI).

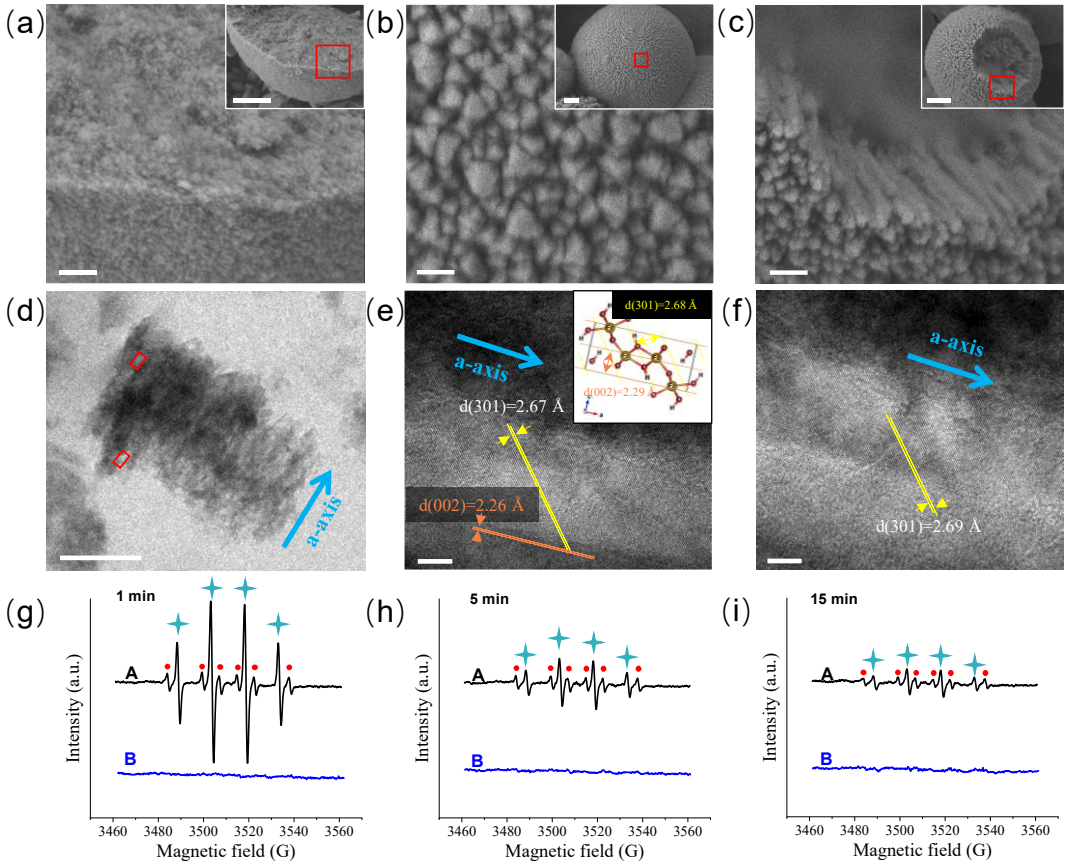


Figure 5. The growth orientation of siderite mineral transformation products induced by humic acid under light. Representative SEM images of siderite (**a**), SHL_{3h} (**b**), and SHL_{1h} (**c**). The representative TEM (**d**) and HRTEM (**e** and **f**) images of the rod-like substances of SHL_{3h}. The schematic diagram of the goethite ([space group *Pnma*] with lattice constants a = 9.91 Å, b = 3.01 Å and c = 4.58 Å) unit cell structure (inset of **e**) was drawn by VESTA software (National Museum of Nature and Science, Japan). The ESR spectra of hydroxyl radical (blue star) and superoxide radical (red dot) in siderite aqueous solution without (A), and with (B), HA under light for 30 min; the samples of 1 min (**g**), 5 min (**h**), and 15 min (**i**) after the reaction were tested by ESR. The initial concentration of siderite was 0.5 g/L, and the initial concentration of HA was 2 mg/L (T=298 K, pH 7). The xenon light intensity was 113.2 $mW \cdot cm^{-2}$. The initial concentration of

dissolved oxygen (DO) was 4 mg/L. The final concentration of DO was 3.1 mg/L. Samples were freeze-dried for 12 h. Scale bars: **a**, **b**, and **c**: 200 nm, inset 1 μm; **d**: 200 nm; **e** and **f**: 5 nm.

To understand how light might influence facet-selective growth, we detected hydroxyl radicals (•OH) and superoxide radicals ($•O_2^-$) in the reaction systems using ESR (Figure 5g-i). In the siderite + light system without HA, both radical signals were detected, with •OH signal intensity approximately 3-fold higher than $•O_2^-$. These radicals likely arise from photo-excitation of Fe(III) species and subsequent Fenton-like reactions. In the presence of HA, radicals were below detection limits, suggesting rapid scavenging by HA or reaction at the mineral surface.

The relationship between radical generation and facet-selective growth is not directly demonstrated by our data, but several plausible mechanisms can be hypothesized. First, radicals could react with surface Fe atoms, creating electron-hole pairs that modify surface charge density. DFT calculations (Figure 2d-g) indicate that the (100) facet has lower initial charge density and poorer electron acquisition ability than the (001) facet, making it potentially more susceptible to radical-induced oxidation. Second, radical-mediated oxidation of surface Fe(II) to Fe(III) could create local supersaturation that favors nucleation on specific facets. Third, radicals may partially oxidize or modify adsorbed HA, altering its facet-specific binding affinity.

We must emphasize that these mechanisms remain speculative. The radicals we detect are short-lived species in solution, and their direct interaction with specific crystal facets cannot be resolved with current techniques. Importantly, we cannot rule out alternative explanations. Light absorption by the semiconductor goethite itself generates electron-hole pairs that could

590 drive facet-specific surface chemistry independently of solution-phase radicals, with the
591 detected radicals being a byproduct rather than the primary mediator. Thus, while our data show
592 an association between light exposure and a-axis growth, the causal pathway remains to be
593 established. Future studies using facet-specific probes or in situ spectroscopy will be needed to
594 definitively elucidate the mechanistic pathway.

595 In conclusion, this result was consistent with the experimental behaviour described above,
596 where, in the presence of light, humic acid induced goethite to grow toward the a-axis, while
597 in the darkness, the growth was toward the c-axis.

598

599 **The growth orientation of goethite under alternating light and dark.** The alternation of
600 light and darkness can easily occur in shallow water environments, which can have a profound
601 influence on mineral growth orientation. In this study (Figure 6), the results showed that the
602 SHL_{3h} $D_{0.5h}$ retained the size of the original siderite sphere, but an obvious phase difference
603 occurred on their surface (Figure 6a). A large quantity of submicron-sized polyhedral subunits
604 (grain sizes range from 300 to 600 nm; Figure 6a) was observed on the surface of SHL_{3h} $D_{0.5h}$.
605 A large quantity of submicron-sized mushroom-shaped subunits (grain sizes range from 0.8 to
606 1.2 μm; Figure 6b) was observed on the surface of SHL_{1h} $D_{0.5h}$. This suggested that the
607 previously observed polyhedral subunits (Figure 6a) were only the head of mushroom-shaped
608 substances. However, a large quantity of spherical substances (diameters range from 20 to 30
609 nm; Figure 6b) was beneath the surface of this new coating (goethite). These spherical
610 substances were similar to the surface appearance of SHD_{3h} (Figure 4c) and SHL_{3h} (Figure 5c).
611 This suggested that these might be a precursor of goethite (ferrihydrite, XPS in Figure S3c, SI).

612 The mushroom-shaped subunits ($SHL_{3h}D_{0.5h}$, Figure 6c and Figure S6, SI) was investigated by
613 TEM. Three regions of the mushroom-shaped subunits, denoted as A (the mushroom tail,
614 Figure S6c, SI), B (the mushroom stem, Figure S6d, SI), and C (the mushroom head, Figure
615 S6e, SI) were selected in Figure 6c, and they were observed by high-resolution TEM images
616 (Figures 6: d to h, Figures S7 to S9, SI). The calculated lattice planes (d(014)=1.75 Å and
617 d(010)=2.51 Å, Figure 6d) and the angle between them in region A (Figures 6c) demonstrated
618 that its major phase was 6-line ferrihydrite (a schematic of the unit cell structure is shown in
619 the inset of Figure 6d). The results suggest that free iron atoms were induced to agglomerate
620 and gradually crystallize to form 6-line ferrihydrite (Figure S7, SI). Furthermore, all the
621 resolved interplanar spacings along the region B (Figures 6c) ranged from 2.66 Å to 2.68 Å
622 (Figures 6e and 6f), which corresponded to (301) lattice planes of goethite ([space group *Pnma*]
623 with lattice constants a = 9.91 Å, b = 3.01 Å and c = 4.58 Å). The Fast Fourier transforms (FFT,
624 inset of Figure 6f) in the region of Figure 6f also coincided with Zone [010] of single crystal
625 goethite. The resolved interplanar spacings (Figure 6g) were 2.23 Å and 2.68 Å at the junction
626 of the mushroom head and the stem, which corresponded to the $(\bar{1}02)$ and (301) lattice planes
627 of goethite, respectively. The calculated lattice planes and the angle between them (Figure 6g)
628 coincided with the schematic of the goethite unit cell structure (inset of Figure 6g). Furthermore,
629 the FFT (inset of Figure 6g) in the region of Figure 6g also coincided with the Zone [010] of
630 polycrystalline goethite (Figure 6g). The results revealed that the goethite grows along the
631 crystallography a-axis in the presence of light (Figure S8, SI). However, no lattice fringe and
632 spot signal of FFT was captured in region C (Figure 6h), which indicated that the structures of
633 the mushroom head were amorphous (Figure S9, SI).

The elements along the regions A, B, and C (line L) were investigated by the TEM-EDS line scan (Figure 6i). According to the relative ratio of Fe/O, line L was divided into three regions A' (Fe/O: about 1.46), B' (Fe/O: about 2.00), and C' (Fe/O: about 1.37). The results suggested that the substance in region C' had the highest oxygen content, followed by region A', and region B' had the lowest. By comparing the oxygen content of ferrihydrite ($Fe_5HO_8 \cdot 4H_2O$), goethite (FeOOH), and $Fe(OH)_3$, it was concluded that region A' mainly contained ferrihydrite, region B' contained goethite, and region C' contained amorphous $Fe(OH)_3$, which was consistent with the TEM, SEM, and XPS analyses. It is worth noting that $Fe(OH)_3$ had the highest carbon content, followed by ferrihydrite, and FeOOH had the lowest. This might be due to the complexation of HA on their surface, and HA was gradually expelled as the crystallization progressed.

In summary, it is evident that in the presence of light and HA, goethite grows along the crystallography a-axis and presents a rod-like structure. In contrast, under dark conditions for a short time, the hydroxide of iron grows in a disorderly manner and presents a polyhedral structure.

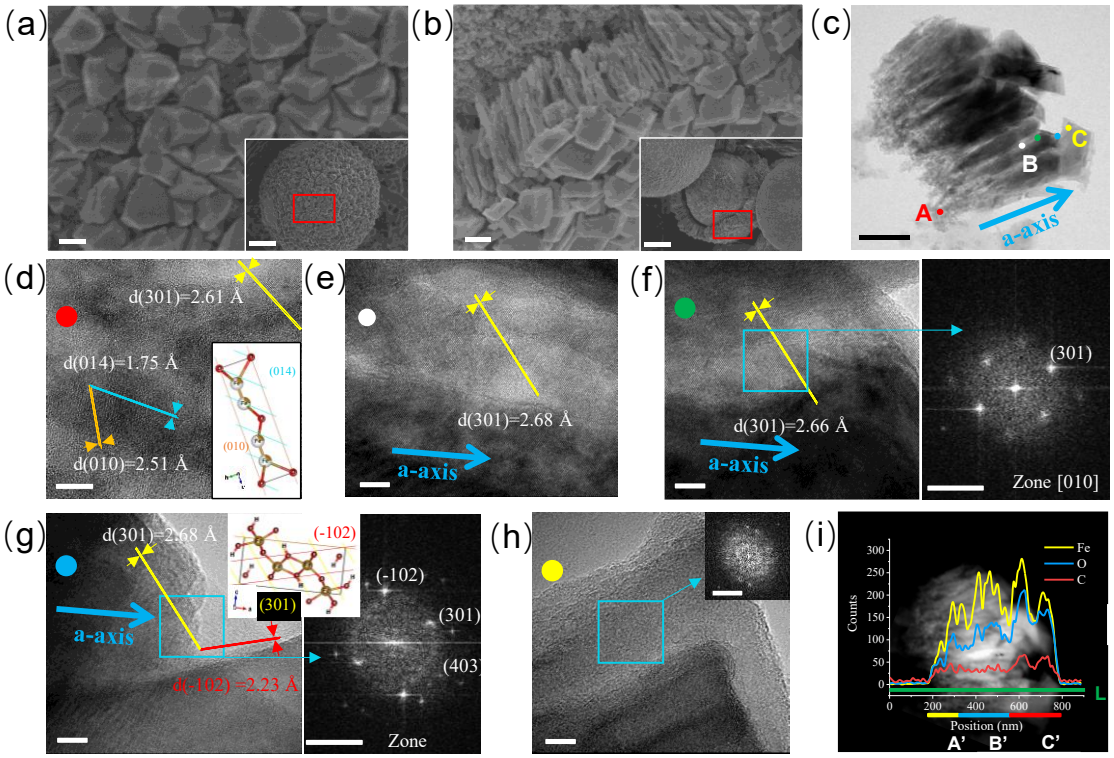


Figure 6. The growth orientation of siderite mineral transformation products induced by humic acid under light for 3 h and then dark for 30 min in succession. Representative SEM images of $SHL_{3h}D_{0.5h}$ (**a**) and $SHL_{1h}D_{0.5h}$ (**b**). Representative TEM image of SHL-3h (**c**) and its HRTEM images (**d**, **e**, **f**, **g**, and **h**); the ball position (Figure 6**c**) corresponded to the HRTEM images of the same ball color in the upper left corner, respectively. Schematic diagrams of the goethite ([space group *Pnma*] with lattice constants a = 9.91 Å, b = 3.01 Å and c = 4.58 Å, the inset of **g**) and ferrihydrite (inset of **d**) unit cell structure, which were drawn by VESTA software (National Museum of Nature and Science, Japan). The insets of, **f**, **g**, and **h,** are the Fast Fourier transforms (FFT) of their corresponding regions. (**i**) Element (Fe, O, and C) line sweep (along the line L from left to right) of the $SHL_{3h}D_{0.5h}$. The initial concentration of siderite was 0.5 g/L, and the initial concentration of HA was 2 mg/L (T=298 K, pH 7). The xenon light intensity was 113.2 $mW \cdot cm^{-2}$. Samples were freeze-dried for 12 h. Scale bars: **a** and **b**: 200 nm, the inset 2μm; **c**: 200 nm; **d**, **e**, **f**, **g**, and **h**: 5 nm; the inset of, **f**, **g**, and **h**: 5 1/nm.

Discussion. The influence of the various factors on crystal growth orientation of Fe-bearing mineral may be related to the gain and loss of electrons on the crystal surface. The results of DFT calculations suggest that it was easy for the goethite crystal to grow perpendicular to (100) lattice planes (TOC and Table S1, SI) by reason of the higher energy released during the

667 elimination of surfaces. However, the factors affecting growth orientation not only include the
668 surface energy of the lattice plane, but also the adsorption energy of organic ligands, and the
669 charge density of unsaturated iron on the lattice plane. In the presence of organic ligands, Fe(II)
670 or light may play a more important role in controlling self-orientation during OA. This leads
671 to the possibility of goethite with different micro-morphologies.

672 Several studies have suggested that -COOH ligands are not only a good stabilizer to prevent
673 the coalescence of nanoparticles, but also influence the morphology by promoting the
674 coalescence of particles on specific surfaces. [1, 2, 15, 25, 26, 28, 29, 56, 63, 84-86] Our DFT calculations
675 employed acetic acid as a simplified model for the carboxylic functional groups in humic acid.
676 While this approach enables rigorous quantum mechanical treatment of carboxyl-Fe
677 interactions, several important deviations from natural HA should be acknowledged. First, HA
678 contains additional functional groups (phenolic OH, quinones, aromatic rings) that may
679 contribute to surface interactions not captured by our model. Second, the macromolecular
680 structure of HA creates steric constraints and multi-point attachment possibilities that differ
681 from simple monodentate binding. Third, the photochemical properties of HA—including light
682 absorption, radical generation, and electron transfer—are more complex than those of acetic
683 acid. However, several lines of evidence suggest that our simplified model captures the
684 dominant binding mechanism: (i) XPS analysis shows carboxyl carbon as the predominant
685 organic functional group associated with the mineral surface; (ii) previous studies have shown
686 that carboxylic acids reproduce the key features of HA adsorption on iron oxides; and (iii) our
687 experimental results with HA are consistent with DFT predictions based on the acetic acid
688 model. Nevertheless, we interpret the DFT results as providing insights into carboxyl-specific

689 binding energetics rather than a complete description of HA-goethite interactions. The
690 calculations of DFT suggest that the -COOH ligand can capture free iron atoms onto the (001)
691 lattice plane by chelation and induce goethite to grow vertically on this surface under dark
692 conditions (Figure 1 and Figure 7). This may be one of the important reasons to explain the
693 growth orientation of goethite parallel to the c-axis in the presence of HA in soil (no light). Our
694 experimental results of Fe(III) matched the predictions of DFT (Figures 1 and 2). However, as
695 an electron donor, Fe(II) is more easily attached to the (001) lattice plane to provide electrons
696 for Fe(III) by reason of the higher charge density and strong electron acquisition ability of this
697 lattice plane (Figure 2d). The experimental results (Figure 3) are consistent with the predictions
698 of DFT. In the presence of Fe(II), the crystal band growing perpendicular to the (001) lattice
699 plane of goethite was formed first, and then the agglomerated Fe ions near the crystal band
700 gradually rearranged and crystallized perpendicular to the (100) lattice plane of goethite under
701 dark conditions (Figure 3). A similar phenomenon has also been observed during the growth
702 process of akageneite. [87] The results suggest that Fe(II) induces goethite to grow along the c-
703 axis and a-axis successively under dark conditions. The critical role of oxygen in the
704 transformation pathway merits emphasis. Under our experimental conditions (DO 4 mg/L,
705 representing air-saturated water), oxidation of Fe(II) to Fe(III) provides the necessary Fe(III)
706 for goethite nucleation and growth. In anoxic sediments, where DO may be depleted, the light-
707 driven transformation pathway described here would be suppressed. This suggests that the
708 photo-controlled facet selection mechanism is most relevant in oxic surface waters and the
709 oxic-anoxic transition zones of shallow sediments, where periodic resuspension exposes
710 minerals to oxygenated water.

711 Light energy (*hv*) can generate free radicals, exciting electron transition on the crystal
712 surface to form electron-holes, which leads to further increase of its surface energy; these
713 surface energies are eliminated subsequently by the aggregation and crystallization. As a result,
714 the crystal grows vertically on these lattice planes. [53, 54] The calculations of DFT predict that
715 light is more likely to excite electron transition on the (100) lattice planes by reason of the
716 lower charge density and poor electron acquisition ability of this lattice plane (Figure 2f). The
717 experimental results (Figures 2 and 3) are consistent with this prediction. In the presence of
718 light, the (100) lattice plane of goethite was more active, and therefore, this lattice plane was
719 gradually eliminated during the growth process, leading to the growth trend along the a-axis of
720 goethite (Figure 7). It should be noted that it is difficult for light, hydroxyl radicals or
721 superoxide radicals to promote the directional crystallization of goethite alone at low intensity,
722 but in the presence of humic acid (HA), they can complete this process in combination. The
723 experimental results show that the influence of light has a leading role in the synergistic effect
724 of light, Fe(II), and HA on crystal growth orientation (Figures 2,3,5 and 6), which is also the
725 main reason for the formation of the mushroom shape. It is evident that in the presence of light
726 and HA, goethite grows along the crystallography a-axis and presents a rod-like structure. In
727 contrast, under dark conditions for a short time, the hydroxide of iron grows in a disorderly
728 manner and presents a polyhedral amorphous structure (Figures 6 and 7).

729 To determine whether the observed differences in phosphate adsorption arise from facet
730 exposure rather than simply differences in surface area, we measured the specific surface areas
731 of Dark-Goe(100) and Light-Goe(001) by N_2-BET analysis. Dark-Goe(100) exhibited a surface
732 area of 98.3 ± 3.2 $m^2 \cdot g^{-1}$, while Light-Goe(001) had a substantially lower surface area of 66.67

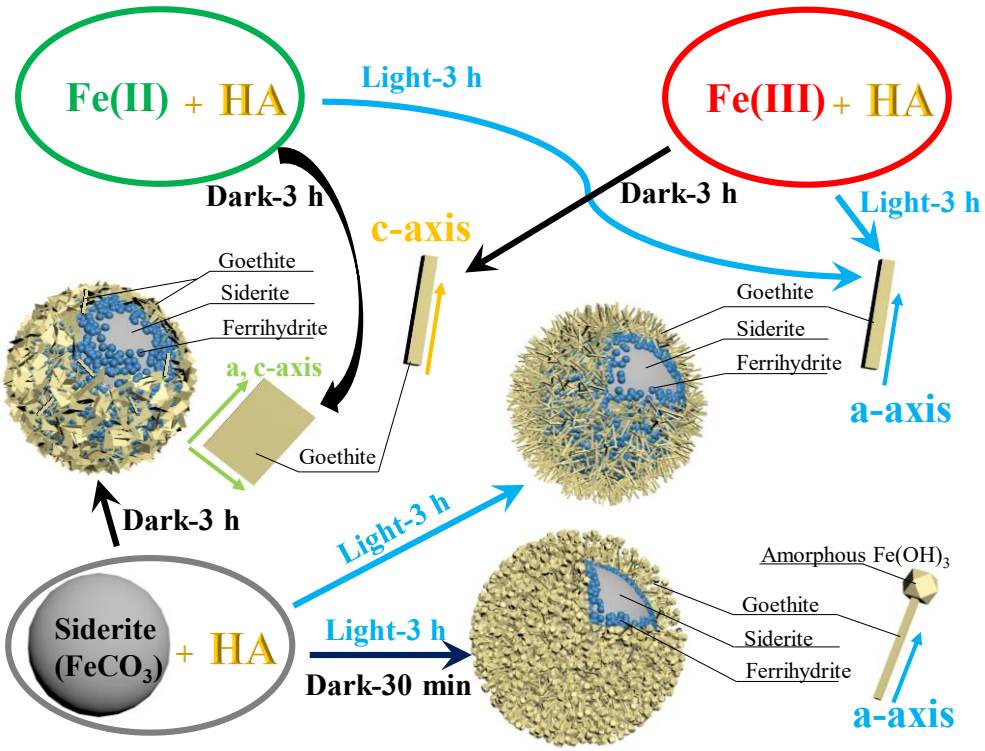
± 2.1 $m^2 \cdot g^{-1}$, consistent with its larger particle size (1-2 μm vs. 100-500 nm). When phosphate adsorption capacity was normalized to surface area, Dark-Goe(100) adsorbed 0.061 mg $P \cdot m^{-2}$ and Light-Goe(001) adsorbed 0.057 mg $P \cdot m^{-2}$ at 24 h. Thus, on a per-unit-area basis, the two materials exhibit remarkably similar adsorption densities, differing by only ~7%. This finding fundamentally revises the interpretation: the 1.5-fold difference in mass-normalized capacity is primarily attributable to differences in specific surface area (driven by particle size and crystallinity) rather than to intrinsic differences in facet-specific reactivity. While both facets are capable of phosphate binding, the (100) facet does not appear to possess inherently higher binding site density per unit area than the (001) facet under the conditions tested.

Taken together, the data suggest a more nuanced picture than a simple facet-controlled adsorption narrative. The surface area-normalized adsorption densities are nearly identical (0.061 vs. 0.057 mg $P \cdot m^{-2}$), indicating that both facets possess comparable intrinsic binding site densities per unit area. The 1.5-fold difference in mass-normalized capacity is therefore primarily a consequence of the larger particle size and lower specific surface area of Light-Goe(001) (66.7 vs. 98.3 $m^2 \cdot g^{-1}$), which in turn reflect the different growth conditions. Crystallinity differences may also contribute: the more crystalline Light-Goe(001) likely has fewer defect sites and grain boundaries that could serve as additional adsorption sites. While surface energy calculations show the (100) facet has slightly higher surface energy (1.22 vs. 1.13 $J \cdot m^{-2}$), this energetic difference does not translate into higher site density per unit area under our experimental conditions. Thus, the primary environmental implication is not that one facet is intrinsically more reactive, but rather that light-driven growth produces larger, more crystalline particles with lower surface area, thereby reducing mass-normalized adsorption

capacity.

In summary, while our data establish a clear correlation between light exposure and a-axis growth orientation, and between facet exposure and phosphate coordination mode, we do not claim to have proven a causal mechanistic pathway. The proposed involvement of radicals in facet-selective growth should be viewed as a testable hypothesis requiring further validation, not as a concluded mechanism. Direct demonstration of radical-mediated facet control would require in situ observations of crystal growth under controlled radical fluxes or facet-specific radical quenching experiments, both of which remain technically challenging. At present, we cannot exclude alternative mechanisms, including light-induced changes in Fe(II)/Fe(III) speciation at the crystal surface, photochemical alteration of HA binding affinity, or indirect effects mediated by changes in solution chemistry. Several important caveats should be considered when extrapolating our laboratory findings to natural systems. First, our experiments employed fixed irradiation intensity (113.2 $mW \cdot cm^{-2}$, approximating midday summer sunlight at 40°N latitude) and continuous exposure, whereas natural systems experience diurnal cycles, variable cloud cover, and spectral attenuation with depth. Second, our simplified system contained only HA as organic matter, whereas natural waters contain diverse organic compounds with varying photochemical reactivities. Third, our experiments were conducted over 3 h, capturing initial crystallization; natural transformation occurs over longer timescales during which multiple light-dark cycles and competing reactions may occur. Fourth, microbial activity, which was absent in our system, may significantly influence Fe cycling and mineral transformation in natural settings. Therefore, while our findings identify a previously unrecognized factor that could influence phosphorus dynamics, the quantitative

777 significance of light-driven facet control in natural systems remains to be determined through
778 field studies.



779

780 **Figure 7. The prominent role of light in goethite growth along a-axis.** Possible pathways of crystal growth
781 orientation during mineral transformation from Fe(II)/Fe(III)/siderite to goethite induced by dark or light
782 with HA.

783

784 **Environmental Implications.** The growth orientation of goethite directly determines
785 which lattice plane will be exposed to the mineral exterior. This will lead to the surface of
786 goethite having different charge densities and surface energies, and different adsorption
787 activities. Our experimental results show that Dark-Goe(100) exhibits 1.5-fold higher mass-
788 normalized phosphate adsorption capacity than Light-Goe(001). However, surface area-
789 normalization reveals that this difference is primarily attributable to the larger particle size and
790 lower specific surface area of Light-Goe(001) (66.7 vs. 98.3 $m^2 \cdot g^{-1}$), rather than to intrinsic
791 differences in facet-specific binding site density. The two materials show nearly identical

792 adsorption densities on a per-unit-area basis (0.061 vs. 0.057 mg P·m^{-2}). The DFT calculations
793 indicate that the (100) facet has slightly higher surface energy (1.22 vs. 1.13 J·m^{-2}), but this
794 energetic difference does not translate into higher site density under our experimental
795 conditions. The XANES results do show differences in phosphate coordination geometry
796 (bidentate vs. monodentate), suggesting that facet identity may influence binding mode even if
797 total site density is comparable. Thus, the environmental implication is not that one facet is
798 intrinsically more reactive, but rather that light-driven growth produces larger, more crystalline
799 particles with lower surface area, thereby reducing mass-normalized adsorption capacity.

800 The potential influence of light-driven facet control on phosphorus cycling may be
801 modulated by water transparency, which is itself affected by climate change and eutrophication.
802 In many shallow lakes, increased phytoplankton blooms and dissolved organic carbon
803 concentrations reduce light penetration (Secchi depth decreasing from >2 m to <0.5 m),
804 potentially diminishing the depth interval over which light-induced facet selection operates.
805 Conversely, in systems where water clarity improves (e.g., through restoration efforts), the zone
806 of light influence may expand. These considerations suggest that the biogeochemical
807 significance of photo-controlled mineral growth may vary both spatially and temporally in
808 response to changing environmental conditions.

809 These findings suggest that diel irradiation cycles may represent an overlooked control on
810 iron (oxyhydr)oxide reactivity in shallow aquatic systems, potentially contributing to observed
811 temporal variations in phosphorus mobility. The relevance of these laboratory observations to
812 natural systems is suggested by the fact that our experimental conditions (HA concentration 2
813 mg/L, pH 7, temperature 298 K) fall within the range of values reported for eutrophic shallow

lakes worldwide. However, we emphasize that this conditional similarity does not constitute validation. Extrapolation to natural systems requires consideration of additional complexities not captured in our experiments, including microbial activity, variable organic matter composition and concentration, competing ions (e.g., sulfate, carbonate), fluctuating redox conditions, and the presence of other Fe-bearing minerals that may interact with goethite. Future studies should examine whether similar facet-selective growth occurs in field-collected sediments subjected to natural light-dark cycles, and should investigate whether the ~7% difference in surface area-normalized adsorption density (which may be within natural variability) has measurable effects on phosphorus mobility at ecosystem scales. Understanding these processes helps to reveal its potential influence on the Fe, P, and N biogeochemical cycles. These processes can also be applied to environmental remediation and nanomaterial synthesis fields.

Acknowledgements

This work was supported by the National Natural Science Foundation of China (Grants 42107224), the Engineering and Physical Sciences Research Council (grant number EP/N010124/1), and Chinese Key Research and Development Plan of the Ministry of Science and Technology (2019YFD1100104 and 2019YFC1906501).

Author contributions

B. X., Q. X., W.Y., N.J.D. G, H.Z., and M.W. have contributed to the design of the study and the critical revision of the article. B. X. Q. X. and X. L. did the experiments, analyzed the data, prepared figures and drafted the article. B.X. and Q. X. contributed equally to the work. W.Y.,

836 N.J.D. G., H. Z., and M.R. W. finished the final version of the manuscript.

837 **Additional information**

838 Competing financial interests: The authors declare no competing financial interests

839 **Appendix A. Supplementary**

840 The Supplementary Information contains 5 Sections, 10 Figures, and 1 Table, as follows:

841 The detailed synthesis process of siderite (Section S1);

842 The calculation of DFT (Section S2);

843 The characterization methods (Section S3);

844 The growth orientation of goethite formed from Fe(III)/Fe(II) crystallization on the surface
845 of siderite induced by humic acid under light (Section S4);

846 Nucleation and growth of goethite induced by light and HA (Section S5);

847 The calculations of DFT to determine the surface and adsorption energies for (001) and
848 (100) surfaces (Table S1);

849 The DFT calculation of the ligand binding configurations (Figure S1);

850 The fluorescence spectra of Fe(II) induced by HA under dark conditions (Figure S2);

851 The Crystallinity and valence of siderite mineral transformation products induced by humic
852 acid (HA) under light and dark (Figure S3);

853 The concentration of Fe in the solution (Figure S4);

854 The transformation products of siderite induced by Fe(II) or Fe(III) under light condition
855 (Figure S5);

856 The characterization of mushroom-shaped substance of SHL_{3h} (Figure S6);

The characterization of mushroom tail substance of SHL_{3h} (Figure S7);

The characterization of mushroom stem substance of SHL_{3h} (Figure S8);

The characterization of mushroom head substance of SHL_{3h} (Figure S9);

Characterization of mesocrystal and the oriented attachment (OA) at the atomic level (Figure S10).

REFERENCES

1. Matamoros-Veloza, A.; Cespedes, O.; Johnson, B. R. G.; Stawski, T. M.; Terranova, U.; de Leeuw, N. H.; Benning, L. G., A highly reactive precursor in the iron sulfide system. *Nat Commun* **2018,** *9*, (1), 3125.
2. Silva, A. K. D.; Ponge, D.; Peng, Z.; Inden, G.; Lu, Y.; Breen, A.; Gault, B.; Raabe, D., Phase nucleation through confined spinodal fluctuations at crystal defects evidenced in Fe-Mn alloys. *Nat Commun* **2018,** *9*, (1), 1137.
3. Cerantola, V.; Bykova, E.; Kupenko, I.; Merlini, M.; Ismailova, L.; Mccammon, C.; Bykov, M.; Chumakov, A. I.; Petitgirard, S.; Kantor, I., Stability of iron-bearing carbonates in the deep Earth's interior. *Nat. Commun.* **2017,** *8*, 15960.
4. Picard, A.; Kappler, A.; Schmid, G.; Quaroni, L.; Obst, M., Experimental diagenesis of organo-mineral structures formed by microaerophilic Fe(II)-oxidizing bacteria. *Nat. Commun.* **2015,** *6*, 6277.
5. Ludwig, J. R.; Zimmerman, P. M.; Gianino, J. B.; Schindler, C. S., Iron(III)-catalysed carbonyl-olefin metathesis. *Nature* **2016,** *533*, (7603), 374-379.
6. Banfield, J. F.; Welch, S. A.; Zhang, H.; Ebert, T. T.; Penn, R. L., Aggregation-based crystal growth and microstructure development in natural iron oxyhydroxide biomineralization products. *Science* **2000,** *289*, (5480), 751-754.
7. Wang, J.; Wu, B.; Zheng, X.; Ma, J. A.; Yu, W.; Chen, B.; Chu, C., Insights into the Crystallinity-Dependent Photochemical Productions of Reactive Oxygen Species from Iron Minerals. *Environ. Sci. Technol.* **2024,** *58*, (24), 10623-10631.
8. Fang, L.; Chi, J.; Shi, Q.; Wu, Y.; Li, F., Facet-dependent electron transfer induces distinct arsenic reallocations on hematite. *Water Res.* **2023,** *242*, 120180.
9. Notini, L.; ThomasArrigo, L. K.; Kaegi, R.; Kretzschmar, R., Coexisting Goethite Promotes Fe(II)-Catalyzed Transformation of Ferrihydrite to Goethite. *Environ. Sci. Technol.* **2022,** *56*, (17), 12723-12733.
10. Yin, D.; Fan, C.; Sun, S.; Dai, Q.; Wang, K., Effect of iron-based materials on sulfide control in sewer systems. *Water Res.* **2026,** *291*, 125231.
11. Wang, L. J.; Putnis, C. V.; Ruiz Agudo, E.; Hovelmann, J.; Putnis, A., In situ imaging of interfacial precipitation of phosphate on goethite. *Environ. Sci. Technol.* **2015,** *49*, (7), 4184-4192.

12. Yuwono, V. M.; Burrows, N. D.; Soltis, J. A.; Lee Penn, R., Oriented aggregation: formation and transformation of mesocrystal intermediates revealed. *J. Am. Chem. Soc.* **2010,** *132*, (7), 2163-2165.
13. Navrotsky, A., Energetic clues to pathways to biomineralization: precursors, clusters, and nanoparticles. *Proc. Natl. Acad. Sci. USA.* **2004,** *101*, (33), 12096-12101.
14. Navrotsky, A., Nanoscale effects on thermodynamics and phase equilibria in oxide systems. *Chemphyschem* **2011,** *12*, (12), 2207-2215.
15. Chassé, A. W.; Ohno, T., Higher molecular mass organic matter molecules compete with orthophosphate for adsorption to iron (oxy)hydroxide. *Environ. Sci. Technol.* **2016,** *50*, (14), 7461-7469.
16. Yang, Y.; Wang, S.; Xu, Y.; Zheng, B.; Liu, J., Molecular-scale study of aspartate adsorption on goethite and competition with phosphate. *Environ. Sci. Technol.* **2016,** *50*, (6), 2938-2945.
17. Frey, P. A.; Reed, G. H., The ubiquity of iron. *ACS Chem. Biol.* **2012,** *7*, 1477-1481.
18. Tagliabue, A.; Bowie, A. R.; Boyd, P. W.; Buck, K. N.; Johnson, K. S.; Saito, M. A., The integral role of iron in ocean biogeochemistry. *Nature* **2017,** *543*, (7643), 51-59.
19. Zou, Y.; Wang, X.; Khan, A.; Wang, P.; Liu, Y.; Alsaedi, A.; Hayat, T.; Wang, X., Environmental remediation and application of nanoscale zero-valent iron and its composites for the removal of heavy metal ions: a review. *Environ. Sci. Technol.* **2016,** *50*, (14), 7290-7304.
20. Okamura, M.; Kondo, M.; Kuga, R.; Kurashige, Y.; Yanai, T.; Hayami, S.; Praneeth, V. K. K.; Yoshida, M.; Yoneda, K.; Kawata, S., A pentanuclear iron catalyst designed for water oxidation. *Nature* **2016,** *530*, (7591), 465-468.
21. Xing, B.; Li, J.; Li, L.; Graham, N. J. D.; Li, X.; Yu, W., Reduced Cytochrome c: Exploring Its Promoting Function in Synergistic Denitrification by Pseudomonas sp. JM-7 and Thiobacillus denitrificans. *Water Res.* **2025,** *285*, 124109.
22. Ren, D.; Zuo, Z.; Ba, X.; He, W.; Yuan, S.; Cen, Y.; Zhang, G.; Xu, J.; Zhang, N.; Sun, Y.; Wang, A.; Cheng, H., Fe(II/III) cycling-based buffering strategy to mitigate sulfide and nitrate overflow in sulfur autotrophic denitrification process under wastewater quality fluctuations. *Water Res.* **2025,** *286*, 124243.
23. Namayandeh, A.; Zhang, W.; Watson, S. K.; Borkiewicz, O. J.; Bompoti, N. M.; Chrysochoou, M.; Penn, R. L.; Michel, F. M., Goethite and Hematite Nucleation and Growth from Ferrihydrite: Effects of Oxyanion Surface Complexes. *Environ. Sci. Technol.* **2024,** *58*, (13), 5952-5962.
24. Penn, R. L., Imperfect Oriented Attachment: Dislocation Generation in Defect-Free Nanocrystals. *Science* **1998,** *281*, (5379), 969-971.
25. Zhang, X.; Shen, Z.; Liu, J.; Kerisit, S. N.; Bowden, M. E.; Sushko, M. L.; De Yoreo, J. J.; Rosso, K. M., Direction-specific interaction forces underlying zinc oxide crystal growth by oriented attachment. *Nat Commun* **2017,** *8*, (1), 835.
26. Zhu, C.; Liang, S.; Song, E.; Zhou, Y.; Wang, W.; Shan, F.; Shi, Y.; Hao, C.; Yin, K.; Zhang, T., In-situ liquid cell transmission electron microscopy investigation on oriented attachment of gold nanoparticles. *Nat Commun* **2018,** *9*, (1), 421.
27. Li, D.; Nielsen, M. H.; Lee, J. R.; Frandsen, C.; Banfield, J. F.; De Yoreo, J. J., Direction-specific interactions control crystal growth by oriented attachment. *Science* **2012,** *336*, (6084), 1014-1018.
28. Kondrat, S. A.; Smith, P. J.; Wells, P. P.; Chater, P. A.; Carter, J. H.; Morgan, D. J.; Fiordaliso, E. M.; Wagner, J. B.; Davies, T. E.; Lu, L., Stable amorphous georgeite as a precursor to a high-activity catalyst. *Nature* **2016,** *531*, (7592), 83.
29. Xu, Y. F.; Tijssen, K. C. H.; Bomans, P. H. H.; Akiva, A.; Friedrich, H.; Kentgens, A. P. M.; Sommerdijk, N. A. J. M., Microscopic structure of the polymer-induced liquid precursor for calcium carbonate. *Nat Commun* **2018,** *9*, (5), 2582.

30. Guo, H.; Ren, Y.; Liu, Q.; Zhao, K.; Li, Y., Enhancement of arsenic adsorption during mineral transformation from siderite to goethite: mechanism and application. *Environ. Sci. Technol.* **2013,** *47*, (2), 1009-1016.
31. Xing, B. B.; Chen, T. H.; Liu, H. B.; Qing, C. S.; Xie, J. J.; Xie, Q. Q., Removal of phosphate from aqueous solution by activated siderite ore: Preparation, performance and mechanism. *J. Taiwan Inst. Chem. E.* **2017,** *80*, 875-882.
32. Gebauer, D.; Cölfen, H., Prenucleation clusters and non-classical nucleation. *Nano Today* **2011,** *6*, (6), 564-584.
33. Zhang, H. Z.; Banfield, J. F., Energy Calculations Predict Nanoparticle Attachment Orientations and Asymmetric Crystal Formation. *J. Phy. Chem. L.* **2012,** *3*, (19), 2882-2886.
34. Zhang, H. Z.; Finnegan, M. P.; Banfield, J. F., Titania nanorods curve to lower their energy. *Nanoscale* **2013,** *5*, (15), 6742.
35. Zhang, H. Z.; De Yoreo, J. J.; Banfield, J. F., A Unified Description of Attachment-Based Crystal. *ACS Nano* **2014,** *8*, 6526-6530.
36. Liu, E.; Pan, Z.; Wang, X.; Chen, Y.; Wang, S.; Liu, P. B.; Liu, Q.; Feng, B.; Wang, X.; Fang, M.; Dong, H.; Bernier-Latmani, R.; Wang, Y.; Wang, Z., Sulfidation Unlocks Dual Reductive Pathways in Uranium Immobilization by Iron Sulfide. *Environ. Sci. Technol.* **2026**.
37. Huang, D.; Ding, L.; Qiu, X.; Zhang, B.; Liang, X.; Guo, X.; Dong, H., Molecular-Scale Insights into the Surface Structural Transformation and Light-Driven Production of Reactive Oxygen Species of Goethite Induced by Microplastic-Derived Dissolved Organic Matter. *Environ. Sci. Technol.* **2025,** *59*, (32), 17349-17360.
38. Ledingham, G. J.; Fang, Y.; Catalano, J. G., Irreversible Trace Metal Binding to Goethite Controlled by the Ion Size. *Environ. Sci. Technol.* **2024,** *58*, (4), 2007-2016.
39. Chaudhary, A.; Usman, M.; Cheng, W.; Haderlein, S.; Boily, J.; Hanna, K., Heavy-Metal Ions Control on PFAS Adsorption on Goethite in Aquatic Systems. *Environ. Sci. Technol.* **2024,** *58*, (45), 20235-20244.
40. Xing, B.; Graham, N. J. D.; Zhao, B.; Li, X.; Tang, Y.; Kappler, A.; Dong, H.; Winkler, M.; Yu, W., Goethite Formed in the Periplasmic Space of Pseudomonas sp. JM-7 during Fe Cycling Enhances Its Denitrification in Water. *Environ. Sci. Technol.* **2023,** *57*, (30), 11096-11107.
41. Kim, Y. Y.; Schenk, A. S.; Ihli, J.; Kulak, A. N.; Hetherington, N. B.; Tang, C. C.; Schmahl, W. W.; Griesshaber, E.; Hyett, G.; Meldrum, F. C., A critical analysis of calcium carbonate mesocrystals. *Nat. Commun.* **2014,** *5*, 4341.
42. Sutter, E.; Sutter, P.; Tkachenko, A. V.; Krahne, R.; De Graaf, J.; Arciniegas, M.; Manna, L., In situ microscopy of the self-assembly of branched nanocrystals in solution. *Nat. Commun.* **2016,** *7*, 11213.
43. Nudelman, F.; Pieterse, K.; George, A.; Bomans, P. H.; Friedrich, H.; Brylka, L. J.; Hilbers, P. A.; De, W. G.; Sommerdijk, N. A., The role of collagen in bone apatite formation in the presence of hydroxyapatite nucleation inhibitors. *Nat. Mater.* **2010,** *9*, (12), 1004-1009.
44. Lupulescu, A. I.; Rimer, J. D., In situ imaging of silicalite-1 surface growth reveals the mechanism of crystallization. *Science* **2014,** *344*, (6185), 729-732.
45. Nielsen, M. H.; Aloni, S.; De Yoreo, J. J., In situ TEM imaging of CaCO3 nucleation reveals coexistence of direct and indirect pathways. *Science* **2014,** *345*, (6201), 1158-1162.
46. Zhu, G.; Sushko, M. L.; Loring, J. S.; Legg, B. A.; Song, M.; Soltis, J. A.; Huang, X.; Rosso, K. M.; De Yoreo, J. J., Self-similar mesocrystals form via interface-driven nucleation and assembly. *Nature* **2021,** *590*, (7846), 416-422.
47. Huang, D.; Ding, L.; Qiu, X.; Zhang, B.; Liang, X.; Guo, X.; Dong, H., Molecular transformation and photochemical reactivity of microplastic-derived dissolved organic matter on goethite: Implications for persistence and reactive oxygen species dynamics. *Water Res.* **2026,** *288*, 124568.

48. Lian, W.; Yu, G.; Ma, J.; Xiong, J.; Niu, C.; Zhang, R.; Xie, H.; Weng, L., Quantitative Insights into Phosphate-Enhanced Lead Immobilization on Goethite. *Environ. Sci. Technol.* **2024,** *58*, (26), 11748-11759.
49. Chen, K.; Guo, C.; Wang, C.; Zhao, S.; Xiong, B.; Lu, G.; Reinfelder, J. R.; Dang, Z., Prediction of Cr(VI) and As(V) adsorption on goethite using hybrid surface complexation-machine learning model. *Water Res.* **2024,** *256*, 121580.
50. Cheng, W.; Li, J.; Sun, J.; Luo, T.; Marsac, R.; Boily, J.; Hanna, K., Nalidixic Acid and Fe(II)/Cu(II) Coadsorption at Goethite and Akaganéite Surfaces. *Environ. Sci. Technol.* **2023,** *57*, (41), 15680-15692.
51. Khare, N.; Martin, J. D.; Hesterberg, D., Phosphate bonding configuration on ferrihydrite based on molecular orbital calculations and XANES fingerprinting. *Geochim. Cosmochim. Ac.* **2007,** *71*, (18), 4405-4415.
52. Nidhi, K.; Dean, H.; James, D. M., XANES Investigation of Phosphate Sorption in Single and Binary Systems of Iron and Aluminum Oxide Minerals. *Environ. Sci. Technol.* **2005,** *39*, 2152-2160.
53. Long, M.; Brame, J.; Qin, F.; Bao, J.; Li, Q.; Alvarez, P. J., Phosphate changes effect of humic acids on TiO_2 photocatalysis: from inhibition to mitigation of electron-hole recombination. *Environ. Sci. Technol.* **2016,** *51*, (1), 514-521.
54. Kim, J. D.; Yee, N.; Nanda, V.; Falkowski, P. G., Anoxic photochemical oxidation of siderite generates molecular hydrogen and iron oxides. *Proc. Natl. Acad. Sci. USA* **2013,** *110*, (25), 10073-7.
55. Shu, Z.; Liu, L.; Tan, W.; Suib, S. L.; Qiu, G.; Yang, X.; Zheng, L.; Liu, F., Solar Irradiation Induced Transformation of Ferrihydrite in the Presence of Aqueous Fe2+. *Environ. Sci. Technol.* **2019,** *53*, (15), 8854-8861.
56. Chen, K. Y.; Chen, T. Y.; Chan, Y. T.; Cheng, C. Y.; Tzou, Y. M.; Liu, Y. T.; Teah, H. Y., Stabilization of natural organic matter by short-range-order Fe hydroxides. *Environ. Sci. Technol.* **2016,** *50*, (23), 12612-12620.
57. Furman, O.; Usenko, S.; Lau, B. L., Relative importance of the humic and fulvic fractions of natural organic matter in the aggregation and deposition of silver nanoparticles. *Environ. Sci. Technol.* **2013,** *47*, (3), 1349-56.
58. Huang, J. H.; Elzinga, E. J.; Brechbuehl, Y.; Voegelin, A.; Kretzschmar, R., Impacts of shewanella putrefaciens strain CN-32 cells and extracellular polymeric substances on the sorption of As(V) and As(III) on Fe(III)-(Hydr)oxides. *Environ. Sci. Technol.* **2011,** *45*, (7), 2804-2810.
59. Johnson, R. L.; Nurmi, J. T.; O'Brien Johnson, G. S.; Fan, D.; O'Brien Johnson, R. L.; Shi, Z.; Salter-Blanc, A. J.; Tratnyek, P. G.; Lowry, G. V., Field-scale transport and transformation of carboxymethylcellulose-stabilized nano zero-valent iron. *Environ. Sci. Technol.* **2013,** *47*, (3), 1573-80.
60. Neil, C. W.; Lee, B.; Jun, Y. S., Different arsenate and phosphate incorporation effects on the nucleation and growth of iron(III) (Hydr)oxides on quartz. *Environ. Sci. Technol.* **2014,** *48*, (20), 11883.
61. Meldrum, F. C.; Cölfen, H., Controlling Mineral Morphologies and Structures in Biological and Synthetic Systems. *Chem. Reviews* **2008,** *108*, 4332-4425.
62. Chen, C.; Hall, S. J.; Coward, E.; Thompson, A., Iron-mediated organic matter decomposition in humid soils can counteract protection. *Nat Commun* **2020,** *11*, (1), 2255.
63. Zierenberg, J.; Schierz, P.; Janke, W., Canonical free-energy barrier of particle and polymer cluster formation. *Nat Commun* **2017,** *8*, 14546.
64. Demichelis, R.; Raiteri, P.; Gale, J. D.; Quigley, D.; Gebauer, D., Stable prenucleation mineral clusters are liquid-like ionic polymers. *Nat. Commun.* **2011,** *2*, (6), 590.
65. Habraken, W. J. E. M.; Tao, J. H.; Brylka, L. J.; Friedrich, H.; Bertinetti, L.; Schenk, A. S.; Verch, A.; Dmitrovic, V.; Bomans, P. H. H.; Frederik, P. M., Ion-association complexes unite classical and non-classical theories for the biomimetic nucleation of calcium phosphate. *Nat. Commun.* **2013,** *4*, (2), 1507.
66. Smeets, P. J. M.; Cho, K. R.; Kempen, R. G. E.; Sommerdijk, N. A. J. M.; De Yoreo, J. J., Calcium carbonate nucleation driven by ion binding in a biomimetic matrix revealed by in situ electron microscopy. *Nat. Mater.* **2015,**

14, (4), 394-399.
67. Xiao, C. l.; Li, M.; Wang, B. j.; Liu, M. F.; Shao, C. Y.; Pan, H.; Lu, Y.; Xu, B.; Li, S.; Zhan, D.; Jiang, Y.; Tang, R.; Liu, X. Y.; Cölfen, H., Total morphosynthesis of biomimetic prismatic-type CaCO3 thin films. *Nat. Commun.* **2017,** *8*, (1).
68. Wiedenbeck, E.; Kovermann, M.; Gebauer, D.; Cölfen, H., Liquid Metastable Precursors of Ibuprofen as Aqueous Nucleation Intermediates. *Angew. Chem. Int. Ed.* **2019,** *58*, (52), 19103-19109.
69. Liu, L.; Nakouzi, E.; Sushko, M. L.; Schenter, G. K.; Mundy, C. J.; Chun, J.; De Yoreo, J. J., Connecting energetics to dynamics in particle growth by oriented attachment using real-time observations. *Nat. Commun.* **2020,** *11*, (1).
70. Zhang, S.; Alberstein, R. G.; De Yoreo, J. J.; Tezcan, F. A., Assembly of a patchy protein into variable 2D lattices via tunable multiscale interactions. *Nat. Commun.* **2020,** *11*, (1).
71. Chen, S.; Li, X.; Battisti, N.; Guan, G.; Montoya, M. A.; Osvatic, J.; Pjevac, P.; Pollak, S.; Richter, A.; Schintlmeister, A.; Wanek, W.; Mussmann, M.; Loy, A., Microbial iron oxide respiration coupled to sulfide oxidation. *Nature* **2025,** *646*, (8086), 925-933.
72. Ma, Z.; Cheng, H., Insights into the Photochemical Mechanism of Goethite: Roles of Different Types of Surface Hydroxyl Groups in Reactive Oxygen Species Generation and Fe(III) Reduction. *Environ. Sci. Technol.* **2024,** *58*, (33), 14812-14822.
73. Hong, Z.; Li, F.; Borch, T.; Shi, Q.; Fang, L., Incorporation of Cu into Goethite Stimulates Oxygen Activation by Surface-Bound Fe(II) for Enhanced As(III) Oxidative Transformation. *Environ. Sci. Technol.* **2023,** *57*, (5), 2162-2174.
74. Xing, B. B.; Ouyang, M. Z.; Graham, N.; Yu, W. Z., Enhancement of phosphate adsorption during mineral transformation of natural siderite induced by humic acid: Mechanism and application. *Chem. Eng. J.* **2020,** *393*, 124730.
75. Xing, B. B.; Graham, N.; Yu, W. Z., Transformation of siderite to goethite by humic acid in the natural environment. *CommsChem* **2020,** *3*, (1).
76. Kresse, G.; Furthmüller, J., Efficient iterative schemes for ab initio total-energy calculations using a plane-wave basis set. *Physical review B* **1996,** *54*, (16), 11169.
77. Kresse, G.; Furthmüller, J., Efficiency of ab-initio total energy calculations for metals and semiconductors using a plane-wave basis set. *Computational materials science* **1996,** *6*, (1), 15-50.
78. Kresse, G.; Hafner, J., Ab initio molecular-dynamics simulation of the liquid-metal–amorphous-semiconductor transition in germanium. *Physical Review B* **1994,** *49*, (20), 14251.
79. Segall, M.; Lindan, P. J.; Probert, M. a.; Pickard, C. J.; Hasnip, P. J.; Clark, S.; Payne, M., First-principles simulation: ideas, illustrations and the CASTEP code. *Journal of Physics: Condensed Matter* **2002,** *14*, (11), 2717.
80. Burleson, D. J.; Penn, R. L., Two-step growth of goethite from ferrihydrite. *Langmuir* **2006,** *22*, (1), 402-409.
81. Tan, B. J.; Klabunde, K. J.; Sherwood, P. M. A., X-ray photoelectron spectroscopy studies of solvated metal atom dispersed catalysts. Monometallic iron and bimetallic iron-cobalt particles on alumina. *Chem.Mater.* **2002,** *2*, (2), 186-191.
82. Tsai, H.; Nie, W.; Blancon, J. C.; Stoumpos, C. C.; Asadpour, R.; Harutyunyan, B.; Neukirch, A. J.; Verduzco, R.; Crochet, J. J.; Tretiak, S.; Pedesseau, L.; Even, J.; Alam, M. A.; Gupta, G.; Lou, J.; Ajayan, P. M.; Bedzyk, M. J.; Kanatzidis, M. G., High-efficiency two-dimensional Ruddlesden-Popper perovskite solar cells. *Nature* **2016,** *536*, (7616), 312-316.
83. Fang, Q.; Chen, B.; Lin, Y.; Guan, Y., Aromatic and hydrophobic surfaces of wood-derived biochar enhance perchlorate adsorption via hydrogen bonding to oxygen-containing organic groups. *Environ. Sci. Technol.* **2014,**

48, (1), 279-88.
84. Li, X.; Qin, F.; Chen, X.; Sheng, A.; Wang, Z.; Liu, J., Dissolution Behavior of Isolated and Aggregated Hematite Particles Revealed by in Situ Liquid Cell Transmission Electron Microscopy. *Environ. Sci. Technol.* **2019,** *53*, (5), 2416-2425.
85. Monteiro, M. J., Order from disorder through dissipation of free energy. *Nat Nano* **2018,** *13*, 770-776.
86. Zhang, X.; He, Y.; Sushko, M. L.; Liu, J.; Luo, L. L.; De Yoreo, J. J.; Mao, S. X.; Wang, C. M.; Rosso, K. M., Direction-specific van der Waals attraction between rutile TiO2 nanocrystals. *Science* **2017,** *356*, 434-437.
87. Chan, C. S.; De Stasio, G.; Welch, S. A.; Girasole, M.; Frazer, B. H.; Nesterova, M. V.; Fakra, S.; Banfield, J. F., Microbial polysaccharides template assembly of nanocrystal fibers. *Science* **2004,** *303*, (5664), 1656-8.